Surface Kinetic Energy Distributions in the North and Equatorial Atlantic Derived from Surface Drifter Observations and High-Resolution Numerical Models with Tidal Forcing

Rémi Laxenaire[1,2], Eric P. Chassignet[2], Xiaobiao Xu[2], Alan J. Wallcraft[2], Luna Hiron[2,3], Brian K. Arbic[4], Maarten C. Buijsman[5], Miguel Solano[5], and Shane Elipot[6]

[1]Laboratoire de l'Atmosphère et des Cyclones (LACy, UMR 8105) CNRS, Université de La Réunion, Météo-France, Saint-Denis de La Réunion, France.
[2]Center for Ocean-Atmospheric Prediction Studies, Florida State University, Tallahassee, FL, USA.
[3]Royal Netherlands Meteorological Institute (KNMI), De Bilt, The Netherlands.
[4]Department of Earth and Environmental Sciences, University of Michigan, Ann Arbor, MI, USA.
[5]School of Ocean Science and Engineering, University of Southern Mississippi, Hattiesburg, MS, USA.
[6]Rosenstiel School of Marine, Atmospheric, and Earth Science, University of Miami, Miami, FL, USA.

Correspondence: Rémi Laxenaire (remi.laxenaire@univ-reunion.fr)

Abstract.

Surface kinetic energy (KE) reflects the distribution of ocean circulation across temporal and spatial scales, shaping energy transfer and mixing in the upper ocean. Quantifying both total KE and its frequency content helps characterize processes from low-frequency motions to tides and near-inertial waves, but KE variability is difficult to quantify with observations alone. High-resolution tidal-resolving ocean models can bridge gaps in our understanding, yet the modeling results depend on the realism of the configuration choices. Focusing on the North and Equatorial Atlantic, we compare surface drifter observations to seven HYCOM high-resolution simulations. We assess model parameters that influence KE across the frequency bands. We first quantify the impact of a Lagrangian versus Eulerian framework in interpreting the KE variability and then perform a series of experiments to quantify the sensitivity of the KE distribution to parameter choices. These experiments show that horizontal resolution is the dominant control for the offshore KE, strongly increasing total and semidiurnal KE, while vertical refinement has a smaller impact offshore, and a stronger impact on the shelf. High-frequency wind forcing amplifies the diurnal and near-inertial variability, while finer bathymetry increases the semidiurnal energy. In contrast, adding wave drag reduces the offshore energy only below the critical latitudes. Overall, the in-depth quantification of the sensitivity of the modeled total KE and its spectral distribution to the parameters offers guidance for setting up high-resolution tide-resolving model experiments.

1 Introduction

Advances in observations and remote sensing have dramatically improved the characterization of ocean velocity fields. For example, geostrophic velocities derived from altimetry provide a global perspective on the geostrophic component of the surface kinetic energy, and have yielded important insights into large-scale to mesoscale motions and their variability (Le Traon, 2013; Abdalla et al., 2021). However, despite recent advances such as Surface Water and Ocean Topography (SWOT) mission

(Morrow et al., 2019; Fu et al., 2024; Archer et al., 2025; Villas Bôas et al., 2025), the spatial and temporal resolution of altimetry remains too coarse to fully resolve smaller oceanographic features and higher frequency motions ($<$100 km, $< days$). Observations of velocities from ADCPs and drifters can capture higher-frequency motions ($\sim hourly$), but these observations are typically limited in duration and geographically sparse.

The advancement of computational capacity has allowed large-scale high-resolution numerical models to include submesoscale motions (Chassignet and Xu, 2017; Ajayi et al., 2020, 2021; Chassignet et al., 2023) and tides (Arbic et al., 2012, 2018; Buijsman et al., 2020; Arbic, 2022; Xu et al., 2022). Numerical models therefore provide a complementary tool to study processes at high temporal and spatial resolution. These models are particularly relevant for the study of high-frequency motions such as internal tides, near-inertial waves, and motions spanning quasi-inertial to low-frequency motions. However, numerical models are, by construction, truncated representations of the ocean, and the modeled circulation is strongly dependent on parameter choices, such as mixing parameterizations and/or horizontal and vertical resolution (e.g., Chassignet and Xu, 2017; Buijsman et al., 2020; Chassignet et al., 2023; Xu et al., 2023; Hiron et al., 2025; Buijsman et al., 2025).

Spectral decomposition of surface currents provides a powerful framework to separate and analyze the distribution of surface kinetic energy (KE) across physically meaningful frequency bands. This approach enables the investigation of key interactions (e.g., wave–current coupling, nonlinear wave–wave transfers), the pathways of energy across scales, and even the tuning of model parameters. Elipot and Lumpkin (2008) and Elipot et al. (2016) first applied rotary spectra to drifter observations, decomposing KE into anticyclonic and cyclonic components that could be mapped into distinct reservoirs of variability to quantify the near surface variability on global scales. Extending this method to model–observation comparisons, Yu et al. (2019) compared a global MIT General Circulation Model (MITgcm) simulation (LLC4320) to surface drifters in waters deeper than 500 m and demonstrated that surface drifters are an efficient database for assessment of the surface circulation predicted by a tide- and eddy-resolving global ocean model. Indeed, they found similar qualitative patterns in KE in both the model and observations, with a dominance of low frequencies and well-defined tidal and near-inertial peaks. Quantitative differences, however, emerged, such as energy deficit (e.g., at low latitudes, and at the near-inertial frequency) or excess (e.g., at the semidiurnal frequency) in the model relative to the observations. Subsequently, Arbic et al. (2022) compared the near-surface KE of another high-resolution global simulation performed with the Hybrid Coordinate Ocean Model (HYCOM) to that of the MITgcm LLC4320 and the drifters KE. The analysis focused on the vertical structure of the near-surface current by comparing results at the surface with those at 15 m depth. They found significant vertical structure in all frequency bands, except the semidiurnal band. The same energy deficit as in Yu et al. (2019) remained present in the models near the equator when compared to observations, but the lack of energy at the near-inertial frequency is less pronounced in HYCOM than in the MITgcm. In addition, the HYCOM semidiurnal KE was found to be closer to those derived from surface drifter observations than the MITgcm semidiurnal KE. Although both Yu et al. (2019) and Arbic et al. (2022) put forward several explanations for the differences between the modeled KE and the KE derived from surface drifter data, they acknowledged the inherent difficulty of comparing fields derived from Eulerian (models) and Lagrangian (observations) velocities. Arbic et al. (2022) also pointed out several limitations in their ocean model comparison, i.e., different forcing and numerical parameters (e.g., vertical

grid resolution, frequency of atmospheric wind forcing, presence or absence of wave drag), outputs from different years, and systematic model errors (e.g., issues with the tidal forcing in the MITgcm LLC4320 simulation).

The differences between Eulerian and Lagrangian estimates of KE were recently investigated by Zhang et al. (2024) and Caspar-Cohen et al. (2024). Zhang et al. (2024) systematically compared Eulerian and Lagrangian estimates of KE by seeding a large ensemble of numerical drifters into the global MITgcm LLC4320 using the v2.0 *Parcels* Python package (Lange and Van Sebille, 2017; Delandmeter and Van Sebille, 2019) and showed that Lagrangian velocity spectra are generally smoother and tend to underestimate KE at low-frequency and in tidal bands, particularly in regions with strong low-frequency KE. Caspar-Cohen et al. (2024) showed that one needs to take into account the distortion introduced by the drifting nature of surface drifters when comparing Lagrangian and Eulerian frequency distribution in LLC4320. Their analysis of the semidiurnal KE levels in the MITgcm LLC4320 and HYCOM simulations are consistent with those of Yu et al. (2019) and Arbic et al. (2022), i.e., that the semidiurnal energy in MITgcm LLC4320 is, on average, about twice that of in situ observations, while HYCOM shows relatively minimal bias overall, though regional variations are apparent.

In this paper, we build on the above studies (Yu et al., 2019; Arbic et al., 2022; Zhang et al., 2024; Caspar-Cohen et al., 2024) to investigate in depth the impact of numerical and forcing parameters on the modeled surface KE. Following the approach of Arbic et al. (2022), we use a suite of tidal-resolving HYCOM simulations of the North and Equatorial Atlantic (Table 1) together with numerical particle experiments, to address several of the limitations that they identified in their study. Specifically, we rely on model–model comparisons between twin experiments, where only a single parameter is varied at a time. This design allows us to isolate the impact of (a) grid resolution (horizontal and vertical), (b) bathymetry resolution, (c) forcing (wind frequency and tidal content), and (d) wave drag and quantify the differences in KE that can be directly attributed to each factor. We also separate our analysis between offshore/deep ocean waters (deeper than $500\,m$) and inshore/continental shelf waters (shallower than $500\,m$). In parallel, we use numerical drifters to further quantify the differences between Lagrangian and Eulerian sampling of velocity fields. The numerical drifters allow us to bridge the two perspectives and link Eulerian-based sensitivity results to observations. Together, these steps provide a clearer attribution of parameter effects, reducing ambiguities in model–observation comparisons, and offering guidance for configuring tide-resolving models capable of reproducing high-frequency surface KE.

The article is organized as follows: Section 2 describes the configurations of the seven HYCOM simulations, the implementation of the numerical drifters, and the surface drifter database used in the comparison. It also introduces the method used to calculate the rotary spectra. In section 3, the surface domain averaged KE from all Eulerian and Lagrangian datasets (numerical and observed) is compared. In Section 4, the Lagrangian spectral estimates from the numerical drifter experiments are (a) compared with that of the surface drifter observations, (b) used to assess the impact of sampling density, and (c) compared with the Eulerian model outputs. In section 5, the impacts of the configuration and parameter choices is quantified using the Eulerian frequency rotary spectra, with separate analyses conducted for deep ocean and continental shelf waters. Specifically, we systematically investigate the impact on the modeled surface KE of the horizontal and vertical resolutions, the number of tidal components, the wave drag, the spatial resolution of the bathymetry, and finally the temporal frequency of wind forcing. By contrasting these experiments with each other, we can directly attribute KE differences to specific changes made between

experiments. Finally, the results are summarized in the concluding section, where we rank the parameters with the most noticeable impact for each frequency band and discuss their relative importance.

2 Data and methods

2.1 Ocean Surface Drifters

We use version 2.01 of the hourly data set from the Global Drifter Program (Elipot et al., 2016, 2022) which includes 15 m-drogued and undrogued drifters. It is important to note that the positioning system used to track the drifters (Argos or GPS) can have an impact on the power spectral density of velocity. Yu et al. (2019) showed that the noise in the Argos positioning system adds high-frequency energy when compared to surface buoys equipped with GPS. In the HYCOM North and Equatorial Atlantic (NEATL) domain, the database of undrogued (drogued) drifters, which was downloaded on 30 April 2025, can be divided into 27,134 (25,956) continuous 60 day segments, each associated with its mean position over the segment duration (Figure 1c), 11,591 (14,933) of these are GPS-tracked drifters.

2.2 HYbrid Coordinate Ocean Model (HYCOM) simulations

The North and Equatorial Atlantic (NEATL) HYCOM experiments, covering the Atlantic from 28°S to 80°N (Figure 1a), are part of a suite of eddying and submesoscale-enabled numerical simulations performed with HYCOM (Bleck, 2002; Chassignet et al., 2003, 2009). These simulations (Chassignet and Xu, 2017; Xu et al., 2022; Chassignet et al., 2023; Xu et al., 2023) were performed to study and quantify the impact of horizontal and vertical resolution on the large-scale circulation and water mass transformations in the Atlantic. In this paper, we analyze three 1/12° horizontal grid-spacing configurations (9 km at the equator, 6 km in the Gulf Stream region) and four 1/50° horizontal grid-spacing configurations (2.25 km at the equator, 1.5 km in the Gulf Stream region). All the simulations are integrated for 18 months with tidal forcing of the eight largest tidal constituents (K_1, O_1, P_1, Q_1, M_2, S_2, N_2, and K_2) after spin-up as described in Xu et al. (2022). The last 12 months outputs are used in the analysis.

These simulations are listed in Table 1, but are described in more details in the following:

- NEATL12-T is the tidal 1/12° reference simulation with 6-hourly atmospheric forcing and 8 tidal constituents.
- NEATL12-M_2 is a twin experiment of NEATL12-T, but with only the semidiunal tidal constituent (M_2).
- NEATL12-T-HVR is a twin experiment of NEATL12-T, but with 96 vertical coordinates instead of 32.
- NEATL50-T is a twin experiment of NEATL12-T, but with a 1/50° horizontal grid-spacing and a coarse bathymetry linearly interpolated from the 1/12° grid-spacing topography of the NEATL12-T (Chassignet and Xu, 2017; Xu et al., 2022; Chassignet et al., 2023). NEATL12-T's bathymetry is based on the 2' Naval Research Laboratory digital bathymetry database, which combines the global topography based on satellite altimetry of Smith and Sandwell (1997) with several high-resolution regional databases.

– NEATL50-T-WD is a twin experiment of NEATL50-T. However, instead of having no wave drag as in NEATL50-T, a Jayne and St. Laurent (2001) internal wave drag with a multiplicative factor of 0.25 is applied to the bottom of the water column (we refer to Buijsman et al. (2015) and Buijsman et al. (2020) for a discussion of this parameter).

– NEATL50-T-HB is a twin experiment of NEATL50-T, but with a 1/50° bathymetry that is derived from the 2019 version of the 15 arc-seconds General Bathymetric Chart of the Ocean data set (GEBCO, 2019) as in Chassignet et al. (2023).

– NEATL50-T-HB-HF is a twin experiment of NEATL50-T-HB, but with higher-frequency, hourly wind stress variability from the National Centers for Environmental Prediction Climate Forecast System Reanalysis (Saha et al., 2010) instead of the 6-hourly wind forcing used in previous experiments.

In the vertical dimension, the above simulations contain 32 or 96 hybrid layers with density referenced to 2,000 m (σ_2) (see Chassignet and Xu (2017) and Xu et al. (2023) for details). The vertical coordinate (Bleck, 2002) is isopycnal in the stratified open ocean and makes a dynamically smooth and time dependent transition to terrain-following coordinates in shallow coastal regions and to fixed pressure levels in the surface mixed layer and/or unstratified seas (Chassignet et al., 2003, 2006). No inflow or outflow is prescribed at the northern and southern boundaries. Within a buffer zone of about 3° from the northern and southern boundaries, the 3-D modeled temperature, salinity, and depth of isopycnal interfaces are restored to the monthly Generalized Digital Environmental Model (GDEM, Teague et al. (1990); Carnes (2009)) climatology with an e-folding time of 5-60 days that increases with distance from the boundary. The initial conditions are derived from the GDEM climatology potential temperature and salinity and the atmospheric forcing is derived from the European Centre for Medium-Range Weather Forecasts reanalysis ERA40 (Uppala et al., 2005) with 6-hourly wind anomalies from the Fleet Numerical Meteorology and Oceanography Center Navy Operational Global Atmospheric Prediction System (Hogan and Rosmond, 1991; Goerss and Jeffries, 1994) for the year 2003. The year 2003 is considered a neutral year over the 1993-present timeframe in terms of long-term atmospheric patterns, such as the North Atlantic Oscillation. The reader is referred to Chassignet and Xu (2017) and Chassignet et al. (2023) for details on the parameterizations used in the model.

To derive surface velocity from particles, and thus simulate the trajectories of surface drifters, we performed an Ocean Parcel experiment using the v2.0 *Parcels* Python package (Lange and Van Sebille, 2017; Delandmeter and Van Sebille, 2019). This Ocean Parcel experiment (hereafter referred to as OP Seed 1/2°) was conducted in the NEATL50-T-HB-HF numerical simulation. Particles were seeded every 30 days on a 1/2° × 1/2° regular grid and tracked for 60 days. This resulted in 11 seeding events over the one-year simulation, yielding 264,361 trajectory segments of 60 days, each associated with its mean position over segment duration (Figure 1b). To assess whether differences between simulated and observed statistics could arise solely from the irregular spatial distribution of real drifter observations, we constructed a subset of the OP Seed 1/2° dataset that replicates the sampling characteristics of the surface drifter dataset (hereafter referred to as OP Seed Drifters). Specifically, for each 1° × 1° bin cell of OP Seed 1/2°, we randomly selected trajectory segments so that the number of simulated segments in that cell match the number of undrogued surface drifter segments observed in the same cell (Figure 1c). In a few cases, the OP Seed 1/2° dataset contained fewer segments than the undrogued drifter dataset for a given cell; in such cases, all available simulated segments were used. This approach keeps the spatial sampling density of the OP Seed Drifters as close as possible

Table 1. Summary of the seven North and Equatorial Atlantic (NEATL) HYCOM simulations (updated from Xu et al. (2022))

Experiment	Horizontal resolution	Numberof layers	Bathymetry resolution	Atmospheric forcing frequency	Number of Tidal constituents	Wave drag
NEATL12-T	1/12°	32	1/12°	6 hours	8	No
NEATL12-M_2	1/12°	32	1/12°	6 hours	1	No
NEATL12-T-HVR	1/12°	96	1/12°	6 hours	8	No
NEATL50-T	1/50°	32	1/12°	6 hours	8	No
NEATL50-T-WD	1/50°	32	1/12°	6 hours	8	Yes
NEATL50-T-HB	1/50°	32	1/50°	6 hours	8	No
NEATL50-T-HB-HF	1/50°	32	1/50°	1 hour	8	No

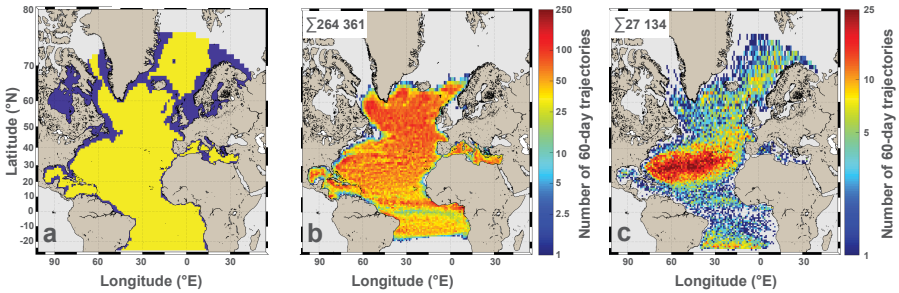


Figure 1. (a) HYCOM NEATL domain in $1^\circ \times 1^\circ$ bins of yellow (blue) regions indicating offshore (inshore) regions in waters deeper (shallower) than $500\,m$. (b) and (c) number of 60-day trajectories in $1^\circ \times 1^\circ$ bin for, respectively, the Ocean Parcel experiment and undrogued surface drifters. The total number of segments is given in the top left of panels b and c.

to that of the observational dataset while avoiding oversampling, ensuring that any differences found in subsequent analyses cannot be attributed to sampling bias. The resulting subset contains 24,302 trajectory segments of 60 days each.

Finally, we divide the NEATL domain into offshore/deep ocean waters and inshore/continental shelf waters (Figure 1a). These sub domains are defined, respectively, as grid points in waters deeper and shallower than $500\,m$ as interpolated from ETOPO1 database (Amante and Eakins, 2009). Yu et al. (2019), Arbic et al. (2022), and Zhang et al. (2024) restricted their analysis to the deep ocean because the geographical distribution of drifters is quite sparse near the coast (Figures 1b,c). For that reason, we also constrain our Lagrangian analysis to the offshore domain. However, when computing the Eulerian fields, both offshore and inshore domains are considered and discussed.

2.3 Analysis methods

Building upon the methodologies outlined in Yu et al. (2019), Arbic et al. (2022), and Zhang et al. (2024), frequency rotary spectra (Gonella, 1972; Mooers, 1973) at each model grid point (Eulerian) and along drifter trajectories (Lagrangian) are computed from surface horizontal velocity time series taken from the HYCOM simulation and surface drifter data. Rotary velocity spectra break down velocity variance into contributions from different frequencies and also separate clockwise from counterclockwise components, thereby distinguishing anticyclonic from cyclonic energy. Following Yu et al. (2019) and Arbic et al. (2022), velocity variance is estimated and interpreted as KE; no factor of $1/2$ is included in the calculations.

To compute spectra, hourly velocity time series (generated at each grid point for the Eulerian estimate and derived from particle velocities for the Lagrangian estimate) are segmented into 60-day periods with a 50% overlap and linearly detrended. For both the model and drifter data, complex-valued fields ($u + iv$, where u and v represent zonal and meridional velocity components, respectively) are multiplied by a Hanning window before computing the 1-D discrete Fourier transform. Spectral estimates are obtained by multiplying the Fourier coefficients by their complex conjugates and averaged over segments. Finally, as per Yu et al. (2019), the rotary frequency spectral densities are adjusted by a factor of $8/3$ to account for the windowing operation (Emery and Thomson, 2001). The resulting Power Spectral Density (PSD) of the rotary spectra corresponds to a 1-year period for the numerical products (both Eulerian and Lagrangian) and spans more than 30 years for the surface drifters (from the end of the 1980s to the beginning of the 2020s).

To decompose KE, the velocity rotary spectra are integrated over four frequency bands: high-frequency ($<$ -0.5 cpd and $>$ 0.5 cpd), near-inertial ($\pm$[0.9, 1.1]f cpd, excluding the $\pm 5^\circ$ latitude band around the equator, with f the Coriolis parameter), semidiurnal ($\pm$[1.9, 2.1] cpd), and diurnal ($\pm$[0.9, 1.1] cpd). In addition to these estimated KE components, the total KE (i.e., the time-mean of the instantaneous values squared) and low-frequency KE (total KE minus high-frequency KE) are computed. It is worth noting that in Arbic et al. (2022), KE maps from drifters were obtained slightly differently: the authors band-pass or low-pass filtered the drifter velocity time series and then computed the variance of the filtered velocities within bins. As stated by Arbic et al. (2022), both methods (Yu et al., 2019; Arbic et al., 2022) yield similar results. This allows us to use the same approach for both Eulerian and Lagrangian fields.

3 Domain averaged surface kinetic energy distributions

In this section, we analyze the rotary velocity spectra and KE integrated over selected frequency bands and over the entire NEATL domain. This analysis provides the baseline for the subsequent detailed comparisons between observed and modeled drifters, Lagrangian and Eulerian estimates, and the twin numerical experiments. The spectra and KE are first averaged within 1°×1° cells and then spatially averaged over the domain using weights proportional to the surface area of each cell.

The rotary spectra for the observed surface drifters, the Ocean Parcel numerical drifters, and the seven HYCOM simulations computed and averaged over the NEATL offshore domain (depth greater than $500\,m$) are displayed in Figure 2. We focus on the offshore domain because the coverage by the observed drifters is sparse in depths less than $500\,m$. The overall pattern is the same for all with a decreasing kinetic energy as the absolute value of the frequency increases and with high energy peaks at

Table 2. Surface kinetic energy (KE; $10^{-3}\ m^2\,s^{-2}$) averaged over the NEATL domain for the seven HYCOM experiments, the Ocean Parcel (OP) experiments, and surface drifters. Two datasets are considered, one that includes GPS-tracked drifters only and one with all drifters (both Argos and GPS positioning systems). Presented below are the total KE, and KE integrated over low-frequency ($>$ -0.5 cpd and $<$ 0.5 cpd); diurnal frequency ($\pm$[0.9, 1.1] cpd); semidiurnal frequency ($\pm$[1.9, 2.1] cpd); and near-inertial frequency ($\pm$[0.9, 1.1]f cpd poleward of $\pm$ 5° latitude). Each cell shows KEd/KEs where KEd and KEs represent KE values computed in waters deeper and shallower than 500 m, respectively. KEs are not provided for Lagrangian fields (i.e., OP and drifters) due to the low density of observations in these regions (Figure 1).

Experiment	Total	Low freq	Diurnal	Semidiurnal	Near-Inertial
NEATL12-T	96.8/134.1	88.8/61.2	1.3/2.0	1.8/64.4	5.9/27.2
NEATL12-M_2	98.1/126.3	90.7/61.5	1.1/0.6	1.6/60.1	5.8/25.5
NEATL12-T-HVR	107.0/151.1	98.4/69.1	1.4/2.1	1.9/72.4	6.4/27.7
NEATL50-T	127.2/144.5	117.3/71.8	1.3/2.2	2.6/62.7	5.3/26.0
NEATL50-T-WD	124.8/140.8	116.4/70.9	1.2/2.1	1.9/60.3	5.1/25.2
NEATL50-T-HB	118.0/136.3	107.9/61.3	1.3/2.0	3.0/65.5	5.3/25.2
NEATL50-T-HB-HF	125.1/143	108.5/64.1	3.0/3.2	3.2/65.2	9.5/27.6
OP Seed 1/2°	122.6/–	107.7/–	3.1/–	2.1/–	9.3/–
OP Seed drifters	122.7/–	101.5/–	3.3/–	2.1/–	9.9/–
Undrogued drifters	139.5/–	103.3/–	2.8/–	1.6/–	8.0/–
Undrogued drifters GPS	150.0/–	92.1/–	3.5/–	1.7/–	8.3/–
Drogued drifters	100.2/–	77.5/–	1.9/–	1.6/–	6.8/–
Drogued drifters GPS	105.3/–	76.4/–	1.9/–	1.8/–	7.7/–

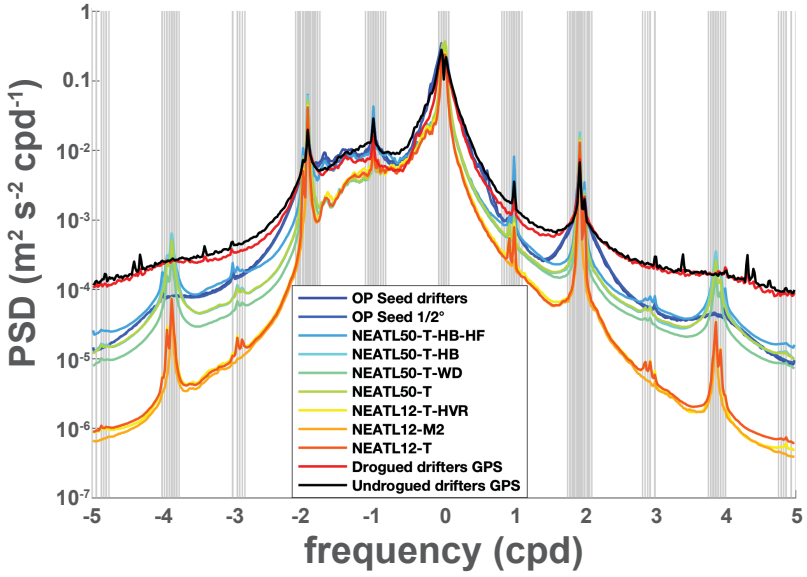


Figure 2. Rotary spectra of kinetic energy averaged over offshore regions for the NEATL domain between -5 and 5 cycles per day (cpd) from the HYCOM simulations, Ocean Parcel (OP) experiments and from surface drifters. Cyclonic and anticyclonic motions are assigned to positive and negative frequencies, respectively. The vertical gray lines indicate tidal frequencies in both positive and negative frequency domains from Arbic et al. (2022). Note the decimal logarithmic scale for the Power Spectrum Density (PSD).

.

the tidal forcing frequencies. Except for the NEATL12-M_2 experiment, which is forced solely by the M_2 tidal constituent, the Eulerian estimates have the same number of peaks in the ± 5 cpd frequency range. The peaks in KE at the higher frequencies are either absent or less marked in the Lagrangian databases (i.e., observed and numerical drifters), in agreement with Arbic et al. (2022). The most notable differences among the datasets is in the level of energy with the highest energy in the observed drifters dataset (drogued and undrogued) and the lowest in the coarse-resolution 1/12° horizontal grid-spacing simulations. There is a significant increase of energy in the 1/50° (Lagrangian and Eulerian) horizontal grid-spacing simulations, but they do not reach the level of the observations.

To obtain a quantitative measure of the differences, we also compute the domain-averaged surface KE components across different frequency bands for all datasets (Table 2). We also differentiate between the continental shelf and open ocean as this distinction will become important in subsequent discussions. Furthermore, in order to compare variations in energy distribution among datasets that do not have the same total energy, we express the energy in each reservoir as a fraction of the total energy (Table 3).

As pointed out by Yu et al. (2019), most of the energy in the offshore domain waters—deeper than 500 m—is contained in the low-frequency band, representing 80–95% of the total KE for the numerical simulations and 60–75% for the drifters (Table 3). This is expected given that large- and mesoscale motions account for most of the oceanic KE (Wunsch and Stammer,

Table 3. Same as in Table 2 but the domain-averaged surface kinetic energy stored in the different reservoir is expressed as a percentage of the total energy, with values separated between waters deeper and shallower than 500 m. Note that the sum of percentages can exceed 100% because the individual frequency bands are derived from velocity variance interpreted as KE.

Experiment	Low freq	Diurnal	Semidiurnal	Near-Inertial
NEATL12-T	91.8%/45.7%	1.3%/1.5%	1.9%/48.0%	6.1%/20.3%
NEATL12-M_2	92.4%/48.7%	1.1%/0.5%	1.7%/47.6%	5.9%/20.2%
NEATL12-T-HVR	91.9%/45.7%	1.3%/1.4%	1.8%/47.9%	5.9%/18.3%
NEATL50-T	92.2%/49.7%	1.0%/1.5%	2.0%/43.4%	4.2%/18.0%
NEATL50-T-WD	93.2%/50.4%	1.0%/1.5%	1.6%/42.9%	4.1%/17.9%
NEATL50-T-HB	91.4%/45.0%	1.1%/1.4%	2.5%/48.0%	4.5%/18.5%
NEATL50-T-HB-HF	86.7%/44.8%	2.4%/2.2%	2.6%/45.6%	7.6%/19.3%
OP Seed 1/2°	87.8%/–	2.5%/–	1.7%/–	7.6%/–
OP Seed drifters	82.7%/–	2.7%/–	1.7%/–	8.1%/–
Undrogued drifters	74.1%/–	2.0%/–	1.2%/–	5.7%/–
Undrogued drifters GPS	61.4%/–	2.3%/–	1.1%/–	5.5%/–
Drogued drifters	77.4%/–	1.9%/–	1.6%/–	6.8%/–
Drogued drifters GPS	72.5%/–	1.8%/–	1.7%/–	7.3%/–

1995; Ferrari and Wunsch, 2009; Morrow and Le Traon, 2012). In contrast, the diurnal, semidiurnal and near-inertial narrower frequency intervals contain between one and two orders of magnitude less energy. Although their fractional contribution is small, high-frequency motions play an important role since they are the main pathways for energy transfer and mixing in the ocean interior (Wunsch and Ferrari, 2004; Müller et al., 2005).

The same variables can be computed in the Eulerian estimates over the continental shelf—waters shallower than 500 m. The shelf results (Table 2) are markedly different, with the energy being higher on average inshore than offshore and with the low-frequency band accounting for only 45–50% of the total (Table 3), leaving considerably more energy associated with higher-frequency motions in inshore areas. There is little difference in the energy between offshore and inshore in the diurnal band, but there is a striking difference in the semidiurnal and near-inertial bands, where the continental shelf can contain up to 35 times more energy than in the open ocean (Tables 2 and 3). Tidal shoaling implies that, as water depth decreases, mass conservation requires higher barotropic velocities and hence larger KE of the barotropic tide, even if a portion of the barotropic energy is converted into internal tides (see demonstration of a tidal wave crossing a slope without reflection or friction in Pugh

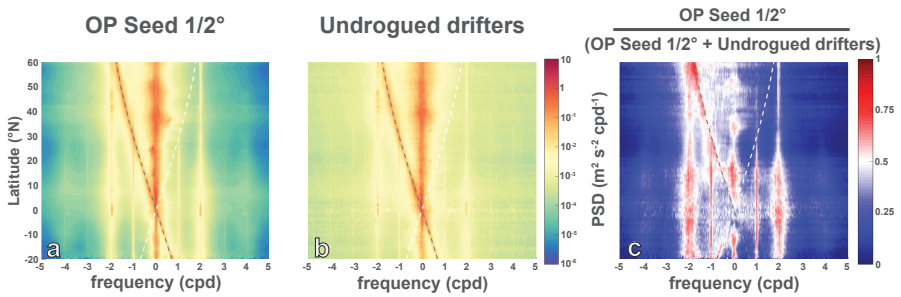


Figure 3. Zonally averaged rotary spectra in 1° latitude bins over regions in waters deeper than 500 m, in the NEATL domain for NEATL50-T-HB-HF computed from Ocean Parcel with a 1/2° seeding (a, first column), from the undrogued drifters (b, second column) and a normalized ratio obtained by dividing the first column by the sum of the first and second columns (c, last column). A ratio of 1/2 means that that the energies are equal. Note the decimal logarithmic color scale for the first and second columns.

and Woodworth, 2014). However, shoaling should affect both the diurnal and semidiurnal bands similarly, which is not what we observe. For instance, in the NEATL domain, several shelf and marginal basins exhibit resonant behavior that selectively amplifies tidal components, depending on their geometry. Diurnal resonances occur in regions such as the Gulf of Mexico (e.g., Grace, 1932), whereas semidiurnal resonances are prominent in the North Sea (e.g., Jänicke et al., 2021), the English Channel and Irish Sea (e.g., Webb, 2013), and the Bay of Fundy–Gulf of Maine system (e.g., Garrett, 1972). Therefore, area-averaged diagnostics cannot fully explain the differences between offshore and inshore energy frequency decomposition.

4 Lagrangian spectral estimates of surface KE

Domain-averaged spectra establish the large-scale structure of surface kinetic energy, but mask important regional and experiment-specific differences. The observations are Lagrangian and are inhomogeneous in space and time. The question then arises as to how spectra computed from a Lagrangian perspective differ from an Eulerian perspective and to what extent we can use observations-based spectra as a reference. To address this, we perform a detailed analysis to evaluate the role of sampling density and quantify the differences in Lagrangian and Eulerian estimates. Specifically, we compare rotary spectra from undrogued drifters with those from numerical particles in the "best" 1/50° experiment (fine bathymetry and hourly winds, NEATL-50-T-HB-HF), which most closely matches observations in the globally averaged rotary spectra of KE (Figure 2).

4.1 Observed versus numerical drifters

In order to compare the surface-advected numerical particles with observations, we focus on undrogued surface drifters, which better capture surface currents than the drogued drifters that were designed to be advected by subsurface currents (Niiler and Paduan, 1995; Lumpkin and Pazos, 2007). It is important to note that there is noise present in the velocity estimates derived from both the GPS- and Argos-tracked drifters. The Argos-tracked drifters exhibit higher noise levels and thus more strongly

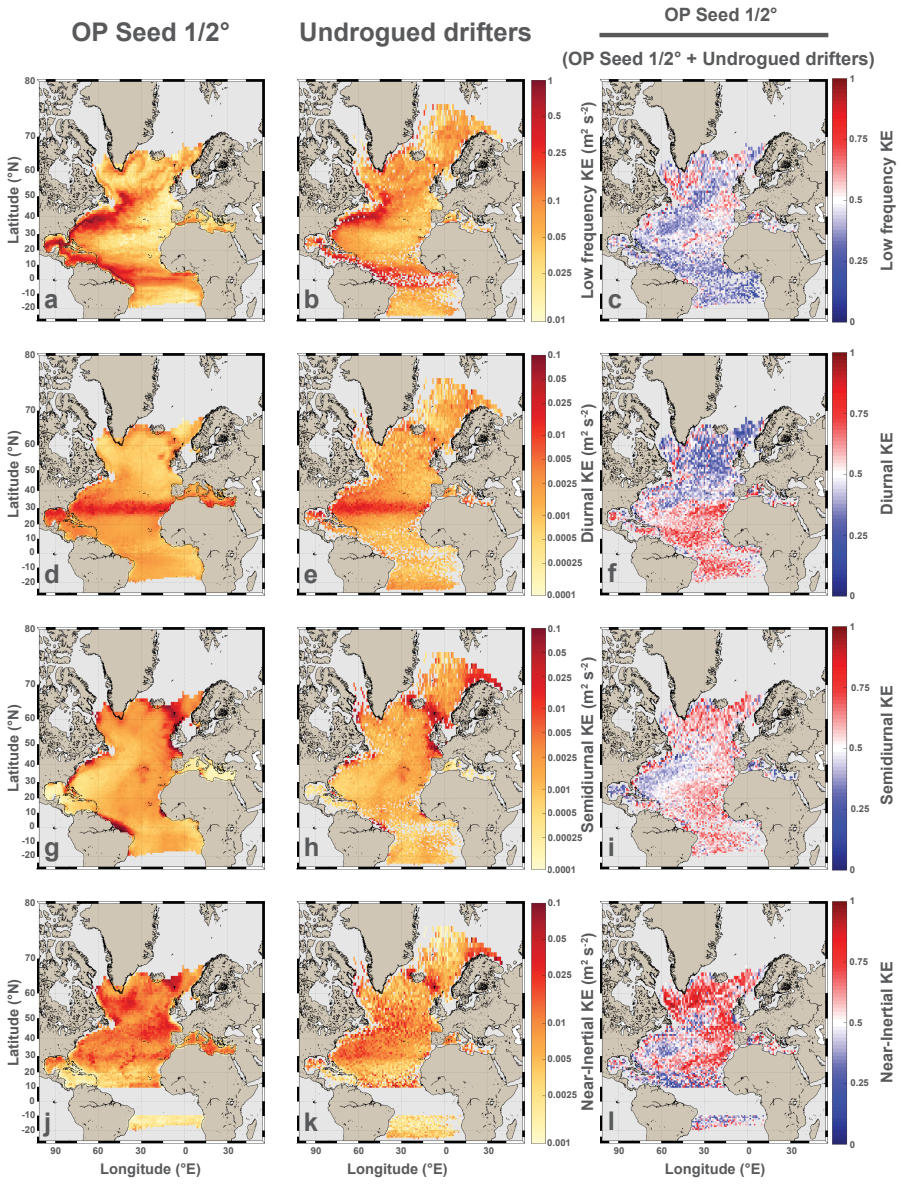


Figure 4. Maps of kinetic energy (KE) components in the NEATL domain for NEATL50-T-HB-HF computed from Ocean Parcel with a 1/2° seeding (a, first column), from the undrogued drifters (b, second column) and a normalized ratio obtained by dividing the first column by the sum of the first and second columns (last column). Maps of low-frequency ($>$ -0.5 cpd and $<$ 0.5 cpd; first row, a to c); Maps of diurnal ($\pm$[0.9, 1.1] cpd; second row, d to f); Maps of semidiurnal ($\pm$[1.9, 2.1] cpd; third row, g to i) and Maps of near-inertial ($\pm$[0.9, 1.1]f cpd out of the band of latitude $\pm 5^{\circ}$ around the equator; fourth row, j to l). A ratio of 1/2 means that that the energies are equal. Note the decimal logarithmic color scale for all the panels.

affect the PSD of rotary spectra Yu et al. (2019). In Figure 2, only the the GPS-tracked drifters were used to minimize the noise impact while, in the rest of this section (Figures 3 and 4), all undrogued drifters are included to have enough segments since we focus on low, diurnal, semi-diurnal and near inertial frequencies.

The zonally averaged rotary spectra are shown in Figure 3. Around 30°N, the natural frequency of near-inertial oscillations (grey line) coincides with the diurnal tidal frequency ($\pm$1 cpd), making it difficult to disentangle their respective impact. This latitude corresponds to the so-called critical latitude, defined as the latitude where the inertial frequency equals the tidal frequency (e.g., Furevik and Foldvik, 1996; Middleton and Denniss, 1993; Robertson, 2001). According to linear internal wave theory, this marks the poleward limit of wave propagation so, above 30°, diurnal internal tides become evanescent. The critical latitude for low-frequency waves ($>$ -0.5 cpd and $<$ 0.5 cpd) lies near 15°, whereas for the semidiurnal ($\pm$2 cpd) band, it is much higher, around 75°, allowing semidiurnal internal waves to propagate across most of the global ocean. The pattern of the zonally averaged PSD of rotary spectra is similar between the observed and numerical drifters (Figure 3). However, the observed drifters show more energy in the high-frequency band, while the semidiurnal and diurnal peaks are, at most latitudinal bands, more pronounced in the NEATL50-T-HB-HF numerical drifters. Overall, the numerical drifters contain less total energy than the observed undrogued surface drifters (Table 2). Yet, they contribute a significantly higher fraction to the low-frequency band, storing more that 80% of the total energy (Table 3). In comparison, the undrogued drifters store 74.1% in the low-frequency (61.4% for GPS-tracked drifters). In absolute and relative terms, the numerical particles exhibit more energy in the semidiurnal and near-inertial bands. The difference in relative term is less marked for diurnal bands so the highest total energy in GPS-tracked drifters results in more energy stored in diurnal band for these observations than for numerical particles.

To assess regional differences, kinetic energy maps are presented in Figure 4. Clear spatial contrasts emerge between the numerical simulation and the observations. At low frequencies, the model indicates higher KE in the center of the North Atlantic whereas the surface drifters show the opposite. In the semidiurnal and near-inertial bands, observations exhibit higher KE in energetic regions such as the Gulf of Mexico and the Gulf Stream, whereas the model distributes energy more broadly. Finally, in the diurnal band, a striking bipolar pattern is found: observations show more KE poleward approximately 30°N, while the model shows more energy equatorward of this latitude. The bipolar pattern in the diurnal band, with more KE poleward of 30°N in the observations but equatorward in the model, echoes the effect of the diurnal critical latitude: diurnal tides are evanescent poleward of around 30°N while near-inertial motions remain energetic there. By contrast, the absence of a comparable cutoff for semidiurnal tides allows them to propagate across the basin, which helps explain their more uniform and dominant imprint in the Eulerian simulations. Once can note that diurnal energy observed north of 30°N is consistent with Arbic et al. (2022), which reported that diurnal motions are driven not only by tides, but also by the day/night solar heating cycle.

In conclusion, the undrogued surface drifter data contains more total energy than numerical particles advected by the model velocity fields. When examining the distribution of energy across frequencies, both datasets show a comparable pattern. However, the model slightly over-represents the fraction of total energy in the near-inertial and semidiurnal reservoirs. Unexpected patterns emerge when scrutinizing the maps. In the near-inertial band specifically, spatial comparisons are hindered by the mismatch in temporal coverage: the observations span 30 years, while the OP drifters reflect variability from a single model year.

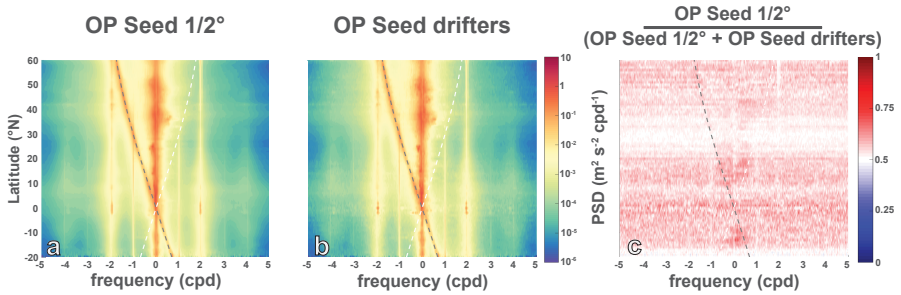


Figure 5. Zonally averaged rotary spectra in 1° latitude bins over regions in waters deeper than $500\,m$, in the NEATL domain for OP Seed $1/2^\circ$ (a, first column), OP Seed drifters (b, second column) and a normalized ratio obtained by dividing the first column by the sum of the first and second columns (c, last column). A ratio of 1/2 means that that the energies are equal. Note the decimal logarithmic color scale for the first and second columns.

For instance, the two narrow bands of enhanced near-inertial energy between 20° and 30°N in panel j of Figure 4 correspond to the tracks of Hurricanes Fabian and Kate of the 2003 season, the atmospheric forcing year of the model simulation (note that this feature is even more apparent in the Eulerian fields shown in panel j of Figure 8).

4.2 Impact of sampling

The above comparison to the observed drifter database was performed with the numerical drifters seeded uniformly on a $1/2^\circ \times 1/2^\circ$ grid for a total of 244,361 trajectory segments. This is a factor of 10 greater than the number of segments (27,134) derived from the observed drifters. We therefore subsampled OP Seed $1/2^\circ$ to match the observed distribution (called OP Seed drifters) and compare the rotary spectra to quantify the impact of the number of drifters on the KE estimates.

When comparing the ratio of the zonally averaged PSD of rotary spectra from OP Seed $1/2^\circ$ to OP Seed drifters (Figure 5), we find no distinct spectral differences, apart from a frequency-independent positive bias in energy for the uniform OP Seed $1/2^\circ$ drifters. The exception is around 30°N where the ratio is near 0.5 which means the energies are nearly equal (Figure 5c). This latitude band corresponds to the location of the North Atlantic gyre where, as shown in Figure 1c, the number of undrogued surface drifters is at a maximum. Thus, the KE level is impacted by the number of surface drifters, but, as shown in Tables 2 and 3, it has a small impact on the KE averaged in our domain of study.

To assess the regional differences of OP seed vs. OP seed drifters, KE maps are presented in Figure 6. As suggested by the zonal averaged studies, the energy level in the North Atlantic Gyre is similar at all the studied frequency bands. Otherwise, the uniform higher density of sampling results in more energy especially close to the coast where the number of available segments of undrogued surface drifters is the lowest (Figure 1c).

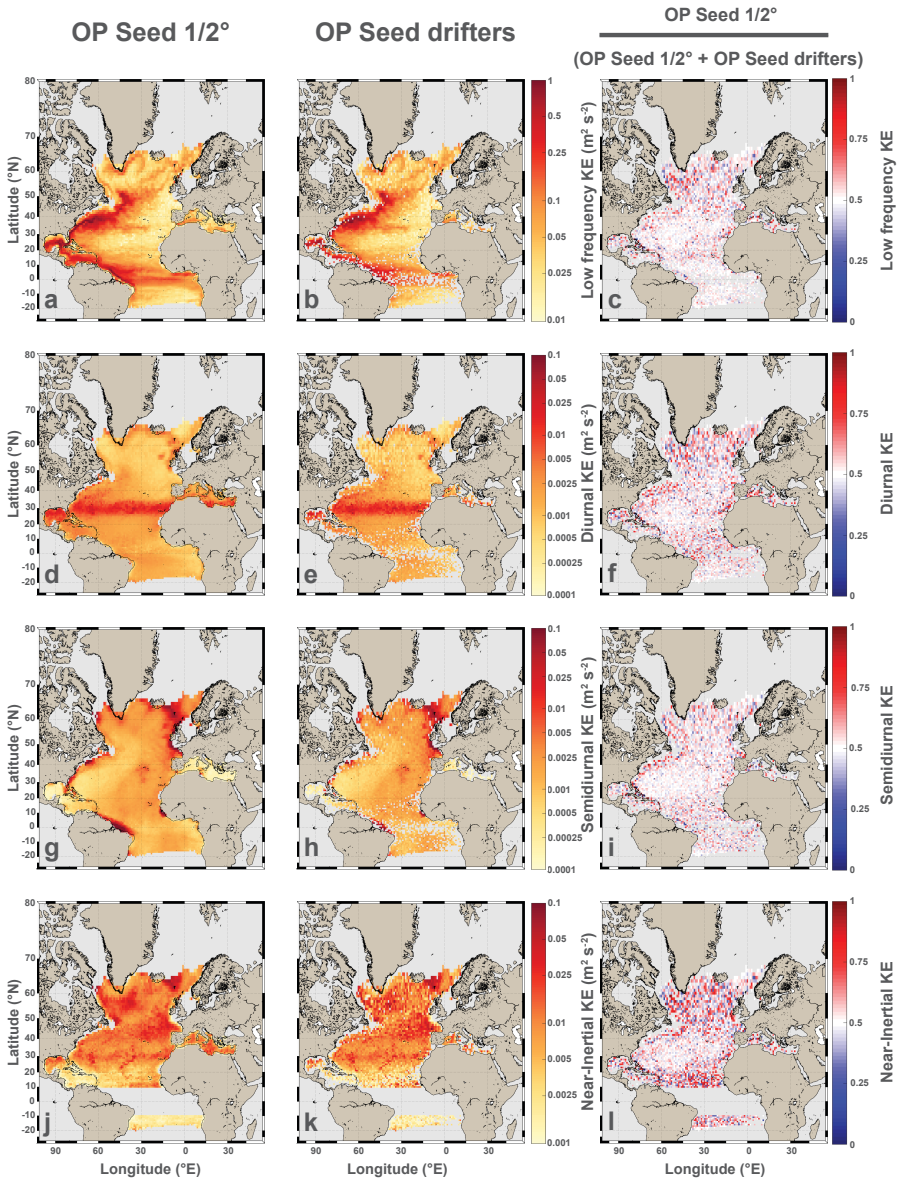


Figure 6. Maps of kinetic energy (KE) components in the NEATL domain for OP Seed 1/2° (first column), OP Seed drifters (second column) and a normalized ratio obtained by dividing the first column by the sum of the first and second columns (last column). Maps of low-frequency ($>$ -0.5 cpd and $<$ 0.5 cpd; first row, a to c); Maps of diurnal ($\pm$[0.9, 1.1] cpd; second row, d to f); Maps of semidiurnal ($\pm$[1.9, 2.1] cpd; third row, g to i) and Maps of near-inertial ($\pm$[0.9, 1.1]f cpd out of the band of latitude $\pm 5^{\circ}$ around the equator; fourth row, j to l). A ratio of 1/2 means that that the energies are equal. Note the decimal logarithmic color scale for all the panels.

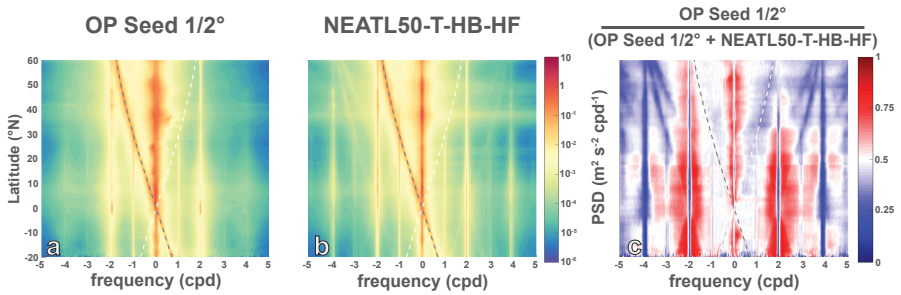


Figure 7. Zonally averaged rotary spectra in 1° latitude bins over regions in waters deeper than 500 m, in the NEATL domain for NEATL50-T-HB-HF computed from Ocean Parcel (Lagrangian, a, first column), from the original grid (Eulerian, b, second column) and a normalized ratio obtained by dividing the first column by the sum of the first and second columns (c, last column). A ratio of 1/2 means that that the energies are equal. Note the decimal logarithmic color scale for the first and second columns.

4.3 Lagrangian versus Eulerian sampling

Although surface drifters serve as the reference in this study, they are Lagrangian platforms, while the primary output from numerical simulations is Eulerian in nature. It is therefore crucial to assess the impact of using Lagrangian versus Eulerian velocities on the computation of the surface KE rotary spectra.

The overall pattern is similar in the zonally averaged PSD of rotary spectra calculated for NEATL50-T-HB-HF from native Eulerian fields and in the Ocean Parcel Experiment (OP Seed 1/2°) (Figure 7a and b). However, the energy peaks are broader with respect to frequency in Lagrangian fields and disappear as the frequency increases. For example, the peaks around ± 4 cpd are barely discernible in the Lagrangian spectra, whereas they are prominent in the Eulerian spectra. This behavior, spreading of energy over broader frequency bands, is consistent with observations from earlier work (Davis, 1983; Middleton, 1985; Zaron and Elipot, 2021; Caspar-Cohen et al., 2022, 2024; Zhang et al., 2024). For frequencies close to these peaks, Lagrangian spectra generally exhibit higher energy as shown by the ratio in Figure 7c. The computation of domain-averaged energy stored in specific frequency reservoirs (absolute in Table 2 and relative in Table 3) show that the different velocities (Lagrangian vs. Eulerian) have minimal impact on total energy and in low, diurnal, and near-inertial bands, with maximum differences around 2%. However, significant deviations occur at higher frequency peaks, with Eulerian velocities containing up to 50% more energy in the semidiurnal frequency band than in Lagrangian velocities. To assess the regional differences, KE maps in Figure 8 show that there is comparable level of energy for low, diurnal and near-inertial frequencies in both datasets. For the semidiurnal frequencies, OP 1/12° has less energy over most of the domain but that is not the case everywhere. In particular, the Amazon Bank is associated with significantly more energy in the Lagrangian experiment.

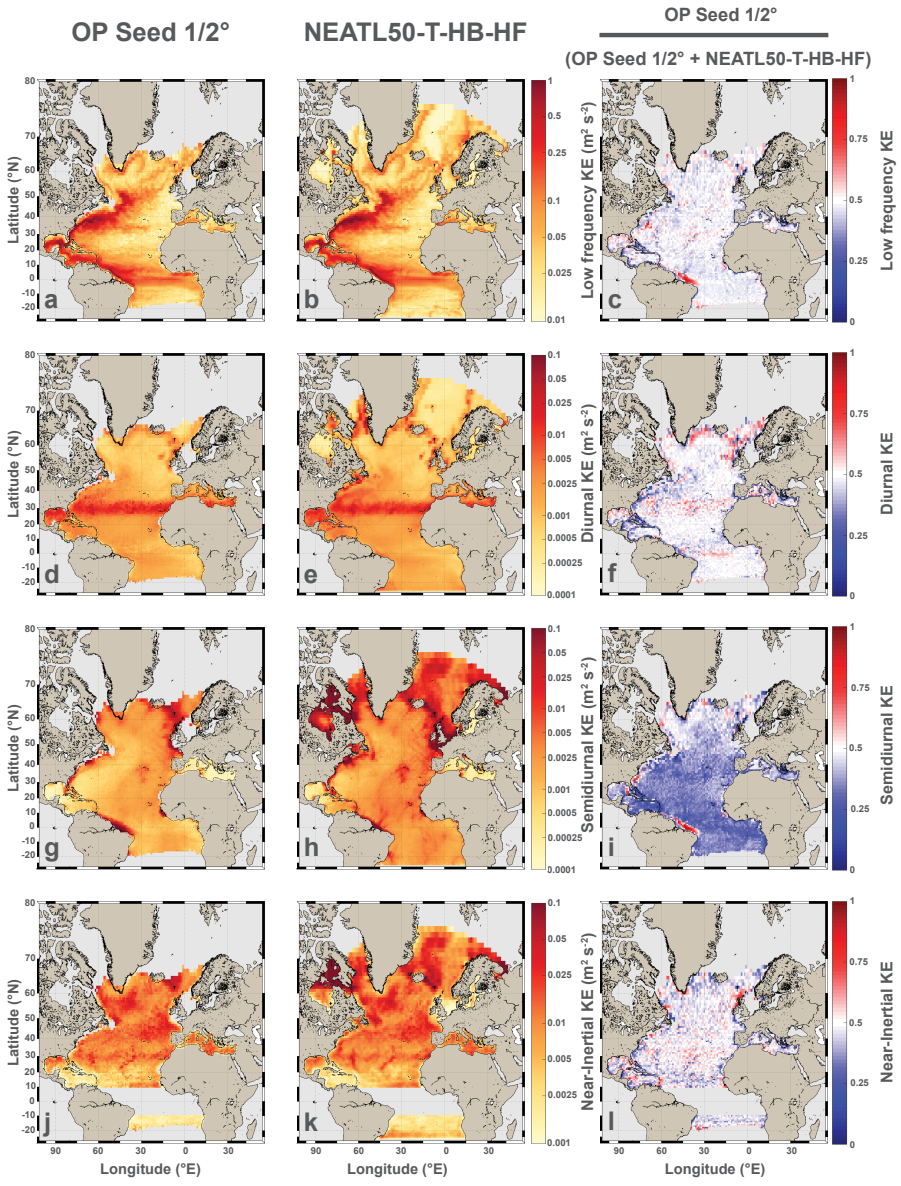


Figure 8. Maps of kinetic energy (KE) components in the NEATL domain for NEATL50-T-HB-HF computed from Ocean Parcel (Lagrangian, first column), from the original grid (Eulerian, second column) and a normalized ratio obtained by dividing the first column by the sum of the first and second columns (last column). Maps of low-frequency ($>$ -0.5 cpd and $<$ 0.5 cpd; first row, a to c); Maps of diurnal ($\pm$[0.9, 1.1] cpd; second row, d to f); Maps of semidiurnal ($\pm$[1.9, 2.1] cpd; third row, g to i) and Maps of near-inertial ($\pm$[0.9, 1.1]f cpd out of the band of latitude $\pm 5^{\circ}$ around the equator; fourth row, j to l). A ratio of 1/2 means that that the energies are equal. Note the decimal logarithmic color scale for all the panels.

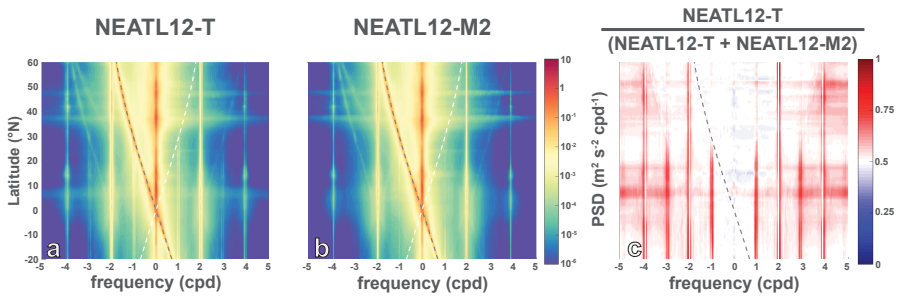


Figure 9. Zonally averaged rotary spectra in 1° latitude bins over regions in waters deeper than 500 m, in the NEATL domain for NEATL12-T (a, first column), NEATL12-M_2 (b, second column) and a normalized ratio obtained by dividing the first column by the sum of the first and second columns (c, last column). A ratio of 1/2 means that that the energies are equal. Note the decimal logarithmic color scale for the first and second columns.

5 Impact of model configuration and parameter choices

The Lagrangian analysis yields three takeaways. First, numerical particles carry less total KE than undrogued drifters and allocate a larger fraction to low frequencies, with relatively more energy in the semidiurnal and near-inertial bands. Second, sampling density has only a minor basin-scale influence. Third, Lagrangian estimates smooth tidal peaks and redistribute variance into the surrounding continuum, yielding substantially less semidiurnal energy than collocated Eulerian estimates. These results leads us to investigate the model parameters that are responsible for model–observation mismatches. We therefore turn to a controlled series of sensitivity experiments that vary a single model parameter at a time to quantify the influence of resolution, tidal content, wind-forcing frequency, bathymetry, and wave drag, respectively.

5.1 Number of tidal components

The pattern of the zonally averaged PSD of rotary spectra calculated in the NEATL12-T and NEATL-12-M_2 experiments, which differ only in the number of tidal components forcing the model, is quite similar overall (Figure 9). However, with additional tidal constituents, NEATL12-T has greater energy in the vicinity of the tidal peaks. This is particularly evident in the ratio plot (Figure 9c), except at the exact position of the M_2 frequency (around ± 2 cpd) and its harmonic (around ± 4 cpd), where the tidal peak of NEATL-12-M_2 is comparable to that of NEATL12-T (i.e., ratio near 0.5). Finally, at lower frequencies, the NEATL-12-M_2 simulation has comparable energy and, even at some specific latitudes in the anticyclonic side (i.e., positive frequencies), slightly more energy. Table 2 shows that reducing the number of tidal components slightly increases the total energy in the open ocean (i.e., averaged offshore KE of 96.810^{-3} $m^2\ s^{-2}$ in NEATL12-T and of 98.110^{-3} $m^2\ s^{-2}$ in NEATL-12-M_2, see Table 2). Conversely, NEATL12-T is more energetic on the continental shelf. The low-frequency component contains a slightly larger fraction of the total energy when fewer tidal components are considered (i.e., 91.8(45.7)% of offshore (inshore) total energy in NEATL12-T and 92.4(48.7)% in NEATL-12-M_2, see Table 3), while, as expected to the

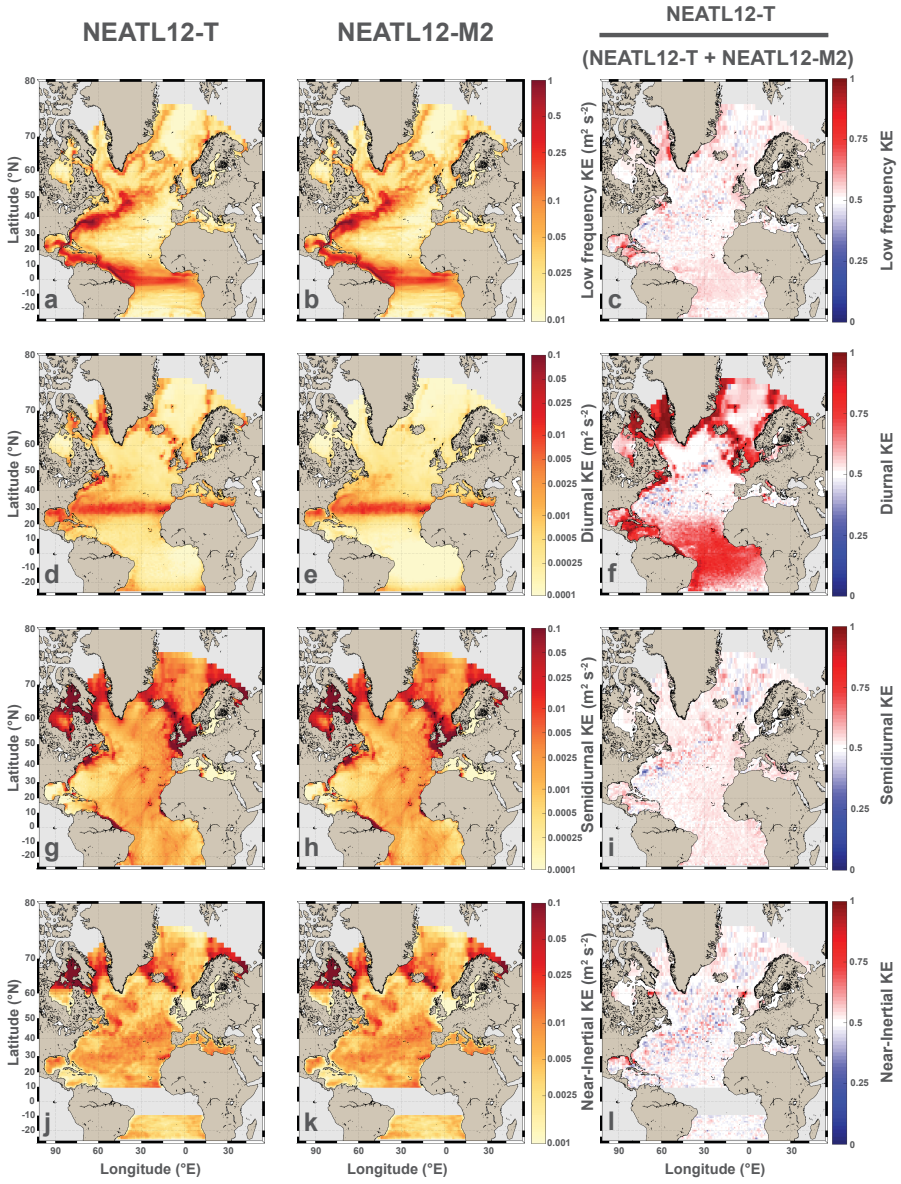


Figure 10. Maps of kinetic energy (KE) components in the NEATL domain for NEATL12-T (first column), NEATL12-M_2 (second column) and a normalized ratio obtained by dividing the first column by the sum of the first and second columns (last column). Maps of low-frequency ($>$ -0.5 cpd and $<$ 0.5 cpd; first row, a to c); Maps of diurnal ($\pm$[0.9, 1.1] cpd; second row, d to f); Maps of semidiurnal ($\pm$[1.9, 2.1] cpd; third row, g to i) and Maps of near-inertial ($\pm$[0.9, 1.1]f cpd out of the band of latitude $\pm 5^{\circ}$ around the equator; fourth row, j to l). A ratio of 1/2 means that that the energies are equal. Note the decimal logarithmic color scale for all the panels.

results of zonally averaged PSD of rotary spectra, the diurnal, semidiurnal, and near-inertial components contain a slightly smaller fraction.

To assess regional differences in KE reservoirs, KE maps over the NEATL domain are shown in Figure 10. Regarding the energy stored in the low frequency band, no clear regional pattern emerges when the number of tidal components is increased (see Figure 10a-c). To assess the regional differences in KE reservoirs, maps within the NEATL domain are presented in Figure 10. Regarding the difference in energy stored at low frequencies, no clear regional difference is observed when the number of tidal components is increased (see Figure 10a-c). One might notice more energy in the NEATL-12-M_2 simulation (blue areas in Figure 10c) in the Gulf of Mexico and near the Gulf Stream, areas known for rich mesoscale eddy activity (e.g., Chelton et al., 2011). In the diurnal band, NEATL12-T contains much more energy than NEATL12-M_2 in the majority of the domain (see Figure 10d-f). This is particularly true close to the coast (3 times more energy both in terms of absolute and percentage of total energy) as NEATL12-M_2 is the experiment with the lowest fraction of total energy stored in the diurnal band (Table 3). Regions such as the Gulf of Mexico, western Caribbean, and Davis Strait, between Greenland and Canada, show much higher energy in the diurnal band associated with the presence of strong diurnal tides in those areas (Gouillon et al., 2010; Baumann et al., 2020). There are exceptions where both experiments have comparable energy, such as the North Atlantic gyre and in the Norwegian, Greenland, and Mediterranean seas, which correspond to the offshore regions at latitude higher than 30° (i.e., diurnal critical latitudes). It is worth noting that the high energy band south of the North Atlantic gyre (visible as a zonal band in Figure 10d-e), around 30°, is expected, as it corresponds to the latitude where near-inertial and diurnal frequencies overlap (Arbic et al., 2022; Raja et al., 2022). NEATL12-T contains slightly more energy in the semidiurnal band than NEATL12-M_2 (Figure 10g-i). As shown in Figure 9c, this is because the energy is distributed over a broader peak near ± 2 cpd in NEATL12-T than in NEATL12-M_2. One possible reason for this broader distribution is that the semidiurnal solar constituent S_2 is combined with M_2 in the NEATL12-T. Another possibility is that the first harmonic of the diurnal frequency is being added to the semidiurnal in NEATL12-T, but not in NEATL12-M_2, but, since there are no differences between open ocean and continental shelf regions, this is unlikely. The distribution and intensity of energy in the near-inertial frequency are very similar between the two experiments, with only small areas where either experiment contains more energy.

In conclusion, adding more tidal components increases the energy at the added peaks as one would expect. However, the impact is not homogeneous over the NEATL. Indeed, this is particularly marked on the continental shelf, where the impact of the tides is the strongest. On the other hand, the experiment with fewer tidal components contains, on average, more energy at low frequencies. This is, however, not uniform across the entire domain, as in some regions like the Labrador Sea, more energy is contained in NEATL12-T than in NEATL12-M_2.

5.2 Horizontal resolution

Examining the zonally averaged PSD of rotating spectra calculated in the NEATL50-T and NEATL12-T experiments, which differ only in horizontal resolution (1/50° and 1/12° horizontal grid-spacing, respectively; Figure 11), shows a clear contrast. The experiment with higher horizontal resolution (NEATL50-T) contains significantly more energy at nearly all frequencies (see Figure 2 of Chassignet and Xu (2017) for a comparison of the time evolution of the domain-averaged total 3D kinetic energy - 1/50° has approximately 70% more energy than 1/12°). This is confirmed by examining the ratio in Figure 11c and particularly true for frequencies whose absolute value exceeds 2 cycles per day. NEATL50-T is more energetic than NEATL12-

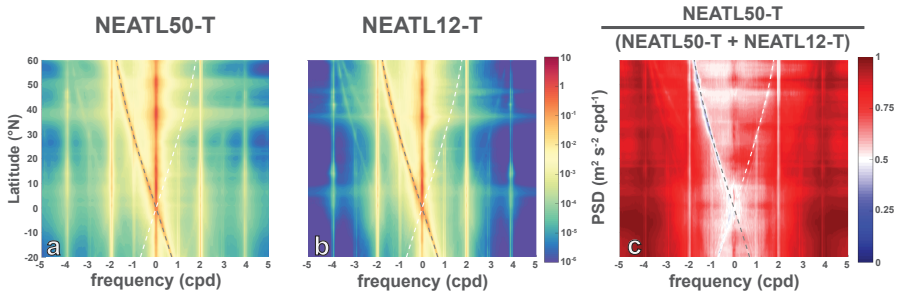


Figure 11. Zonally averaged rotary spectra in 1° latitude bins over regions in waters deeper than 500 m, in the NEATL domain for NEATL50-T (a, first column), NEATL12-T (b, second column), and a normalized ratio obtained by dividing the first column by the sum of the first and second columns (c, last column). A ratio of 1/2 means that that the energies are equal. Note the decimal logarithmic color scale for the first and second columns.

T at exactly ± 2 cpd, but the differences are small in the vicinity of these peaks. The only exception to the rule that higher resolution yields higher energy is that NEATL12-T has more energy in the near-inertial frequency band north of 10°N.

Table 2 shows that the surface energy in the open ocean increases by around one-third when the horizontal resolution increases from 1/12° to 1/50° horizontal grid-spacing; however, the differences are less pronounced on the continental shelf. The excess of energy is, roughly, well distributed across the different reservoirs, as the percentage of the total energy stored in each compartment is comparable between the two experiments (Table 3). In detail, the most noticeable difference occurs in the open ocean where the percentage of total energy stored in the near-inertial band decreases by one-third (from 6% to 4%) as the resolution increases.

To assess the regional differences in details, maps are presented in Figure 12. The NEATL50-T simulation has significantly more energy than NEATL12-T at low, diurnal, and semidiurnal frequencies. However, the opposite is true for the near-inertial frequency. By contrast, near 30° latitude in the diurnal band, NEATL12-T has more energy than NEATL50-T, but this corresponds to the latitude where energy stored in the near-inertial band overlaps with that in the diurnal band (Arbic et al., 2022; Raja et al., 2022).

In conclusion, increasing the horizontal resolution leads to a substantial increase in total energy across most of the energy spectrum, consistent with previous studies. Chassignet et al. (2020) showed that high horizontal-resolution simulations have much higher values of kinetic energy for low frequency motions compared to low-resolution simulations. For tidal frequencies, Buijsman et al. (2020) find that decreasing the horizontal grid-spacing in realistic HYCOM simulations from 8 to 4 km increased the semidiurnal barotropic-to-baroclinic tidal conversion by 50%, and more baroclinic modes were resolved, from 1-2 to 1-5 modes. Nelson et al. (2020) also found that decreasing the horizontal grid spacing, in this case in the regional Massachusetts Institute of Technology general circulation model (MITgcm) simulations, led to more realistic internal wave frequency spectra. The increase in horizontal resolution also leads to a better representation of the submesoscale field, and increases wave-mean and wave-wave interactions, thus explaining the increase in energy between peaks in the simulations

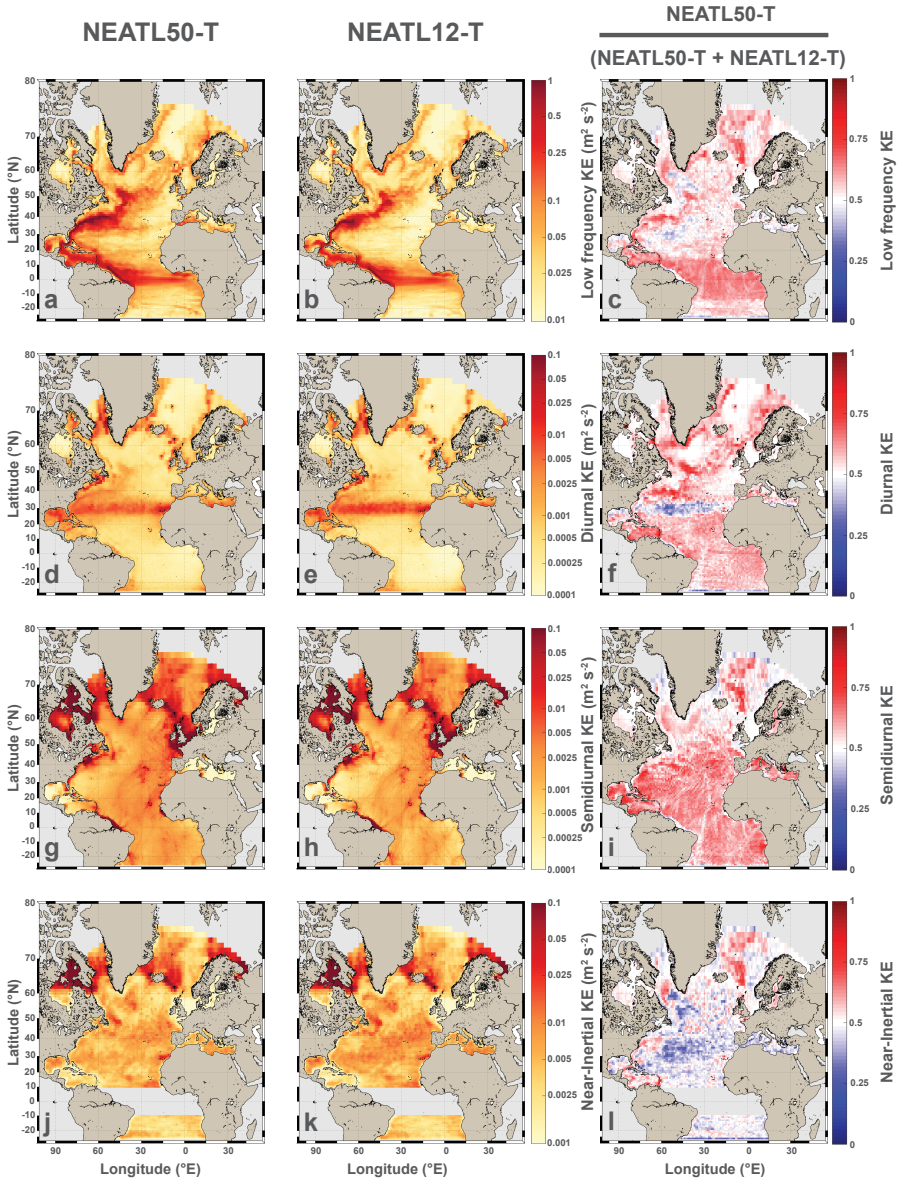


Figure 12. Maps of kinetic energy (KE) components in the NEATL domain for NEATL50-T (first column), NEATL12-T (second column) and a normalized ratio obtained by dividing the first column by the sum of the first and second columns (last column). Maps of low-frequency ($>$ -0.5 cpd and $<$ 0.5 cpd; first row, a to c); Maps of diurnal ($\pm$[0.9, 1.1] cpd; second row, d to f); Maps of semidiurnal ($\pm$[1.9, 2.1] cpd; third row, g to i) and Maps of near-inertial ($\pm$[0.9, 1.1]f cpd out of the band of latitude $\pm 5^\circ$ around the equator; fourth row, j to l). A ratio of 1/2 means that that the energies are equal. Note the decimal logarithmic color scale for all the panels.

with 1/50° horizontal grid-spacing compared to those with 1/12° horizontal grid-spacing (Figure 11c). The only exception is in the near-inertial frequency band, where increasing the horizontal resolution results in a slight reduction of energy on average.

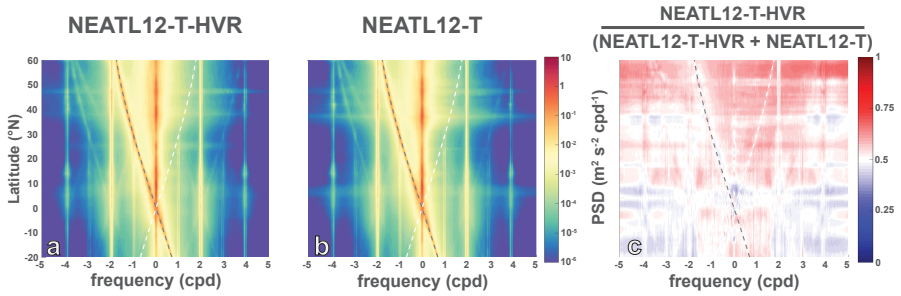


Figure 13. Zonally averaged rotary spectra in 1° latitude bins over regions in waters deeper than 500 m, in the NEATL domain for NEATL12-T-HVR (a, first column), NEATL12-T (b, second column) and a normalized ratio obtained by dividing the first column by the sum of the first and second columns (c, last column). A ratio of 1/2 means that that the energies are equal. Note the decimal logarithmic color scale for the first and second columns.

Furthermore, even though the energy in the semidiurnal frequency band is close in the two simulations, the increase in total energy with higher resolution results in a markedly lower fraction of energy being associated with diurnal variability in the near-shore domain.

5.3 Vertical resolution

Examining the zonally averaged rotating spectra calculated in the NEATL12-T-HVR and NEATL12-T experiments, which differ only in vertical resolution (32 and 96 vertical levels, respectively; Figure 13), no clear differences emerge in either the total energy or the tidal peaks and harmonics. However, the ratio of the two indicates slightly more energy in the northern hemisphere with more vertical levels (NEATL12-T-HVR) and less energy in the southern hemisphere. As seen in Table 2, increasing the vertical resolution from 32 to 96 levels results in a around 10 to 15% increase in total energy, with the increase being higher over the continental shelf. This results in more energy in the different band-integrated KE components which is, as the fraction of total energy does not change much (Table 3), distributed over the frequency domain. The most remarkable difference seen here is that, by increasing the vertical resolution, around 2% less of the total energy is stored in the near-inertial frequencies.

To assess the regional differences in detail, kinetic energy maps are presented in Figure 14. As with global integrals, the regional surface kinetic energy fields increase slightly with higher vertical resolution in the studied frequency ranges, particularly at low frequencies, where the differences can be substantial in some areas, such as the Gulf of Mexico. The increase in energy associated with higher vertical resolution is less pronounced for diurnal, semidiurnal, and near-inertial frequencies, although the increase is more uniform in the diurnal frequency band at the exception, again, of the 30°N latitudinal band. For high-frequency (supertidal) internal gravity waves, Nelson et al. (2020) finds that the modeled internal wave frequency spectra is improved with increased vertical resolution only when the horizontal resolution is also increased. In an idealized 1/100° HYCOM configuration forced solely by semidiurnal tides, Hiron et al. (2025) find that increasing the number of isopycnal layers

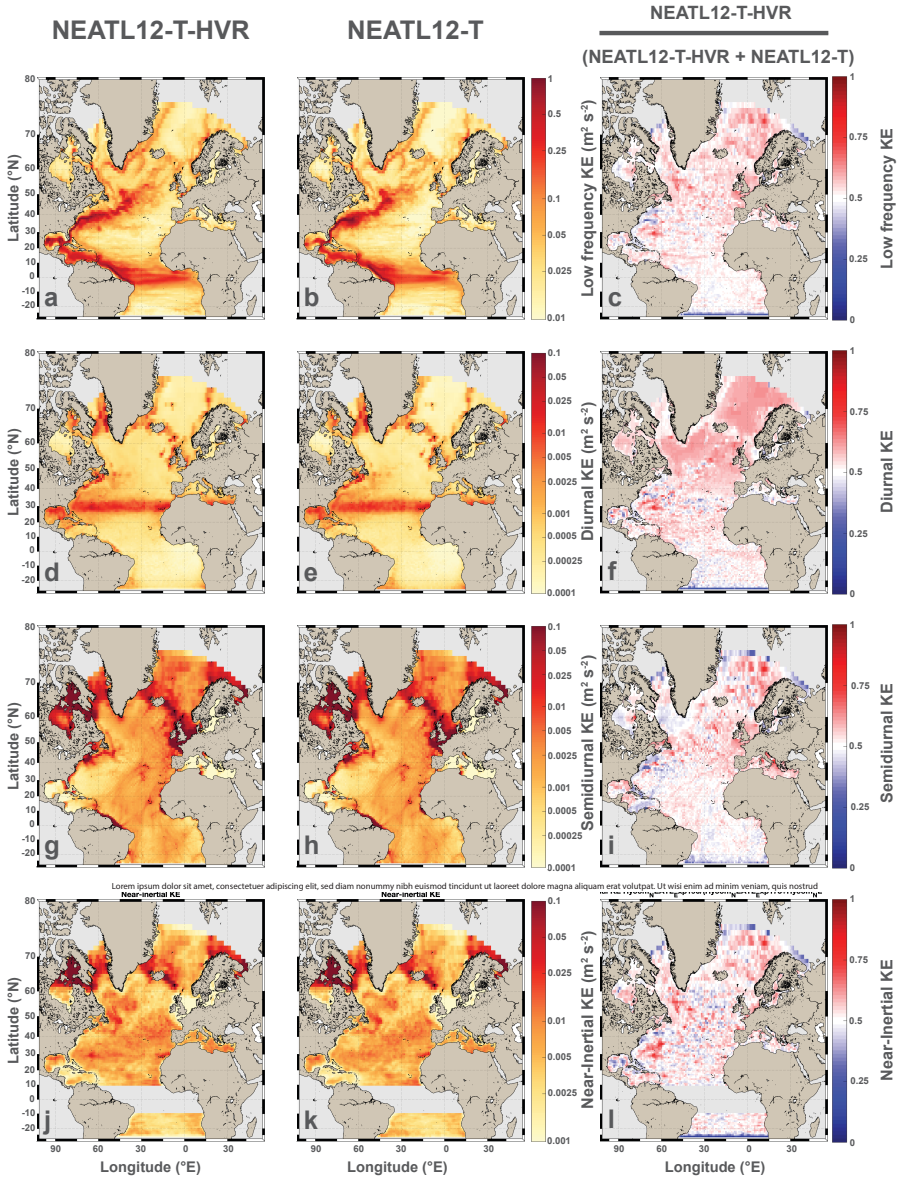


Figure 14. Maps of kinetic energy (KE) components in the NEATL domain for NEATL12-T-HVR (first column), NEATL12-T (second column) and a normalized ratio obtained by dividing the first column by the sum of the first and second columns (last column). Maps of low-frequency ($>$ -0.5 cpd and $<$ 0.5 cpd; first row, a to c); Maps of diurnal ($\pm$[0.9, 1.1] cpd; second row, d to f); Maps of semidiurnal ($\pm$[1.9, 2.1] cpd; third row, g to i) and Maps of near-inertial ($\pm$[0.9, 1.1]f cpd out of the band of latitude $\pm 5^{\circ}$ around the equator; fourth row, j to l). A ratio of 1/2 means that that the energies are equal. Note the decimal logarithmic color scale for all the panels.

increases tidal-induced vertical velocities and available potential energy, while tidal kinetic energy remains largely unchanged. The energetics increase up to 48 layers and change little thereafter. These studies show that tidal energetics among simulations

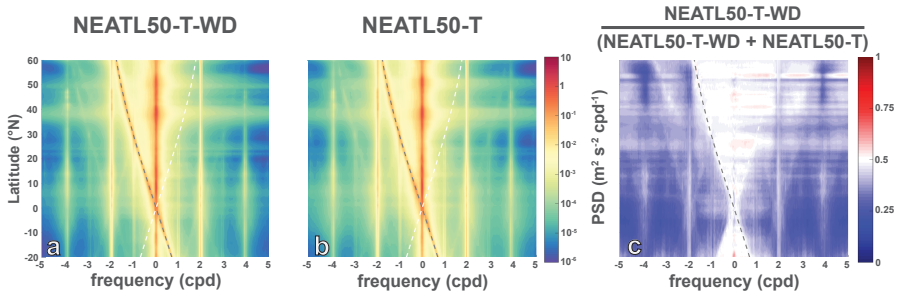


Figure 15. Zonally averaged rotary spectra in 1° latitude bins over regions in waters deeper than 500 m, in the NEATL domain for NEATL50-T-WD (a, first column), NEATL50-T (b, second column) and a normalized ratio obtained by dividing the first column by the sum of the first and second columns (c, last column). A ratio of 1/2 means that that the energies are equal. Note the decimal logarithmic color scale for the first and second columns.

with different number of layers vary as long as horizontal grid-spacing is not limiting. Here, for 1/12° horizontal grid-spacing, the minimal changes in semidiurnal energy between the simulation with 32 and 96 layers might suggest that the horizontal grid-spacing is limiting, or that kinetic energy in the semidiurnal frequency is not significantly impacted by changes in vertical number of layers.

In conclusion, increasing the vertical resolution results in a increase in energy which is distributed over the frequency domain (see also Figure 2).

5.4 Impact of topographic wave drag

Zonally averaged rotary spectra from the NEATL50-T-WD and NEATL50-T experiments, which differ only by the inclusion of wave drag in NEATL50-T-WD, are shown in Figure 15. The addition of wave drag results in a reduction of energy across the majority of the frequency domain. The differences are less pronounced in frequencies lower than the near-inertial frequency, where the differences are almost negligible. Table 2 confirms that the inclusion of wave drag leads to a slight decrease in energy across all the frequency bands analyzed. The most significant impact is observed in the semidiurnal frequency within the offshore domain, where the addition of wave drag results in an energy reduction of approximately 25%, while differences, although present, are less pronounced inshore.

To assess regional variations, KE maps are displayed in Figure 16. These maps confirms that incorporating wave drag leads to a overall reduced surface KE across the frequency bands studied. In the diurnal band, the reduction is most apparent equatorward of 30°N, while no clear signal emerges poleward of this latitude, where diurnal tides become evanescent. In contrast, the decline in semidiurnal energy is more pronounced in the open ocean at nearly all latitudes. Finally, in the near-inertial band, no clear signal emerges.

In conclusion, the inclusion of wave drag results in reduced energy in the frequency bands located below their respective critical latitudes, that is, around ±15° for the low-frequency band, ±30° for the diurnal band, and almost the entire domain for

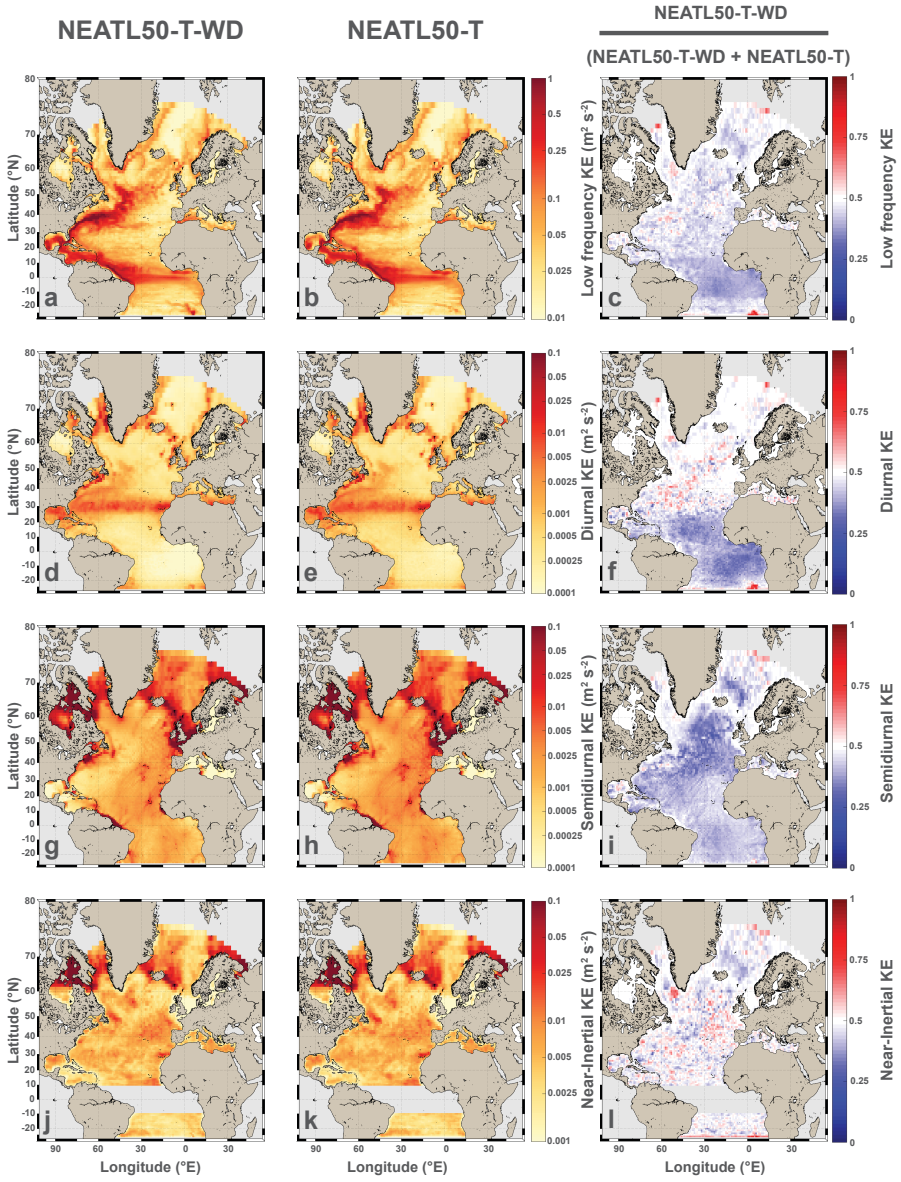


Figure 16. Maps of kinetic energy (KE) components in the NEATL domain for NEATL50-T-WD (first column), NEATL50-T (second column) and a normalized ratio obtained by dividing the first column by the sum of the first and second columns (last column). Maps of low-frequency ($>$ -0.5 cpd and $<$ 0.5 cpd; first row, a to c); Maps of diurnal ($\pm$[0.9, 1.1] cpd; second row, d to f); Maps of semidiurnal ($\pm$[1.9, 2.1] cpd; third row, g to i) and Maps of near-inertial ($\pm$[0.9, 1.1]f cpd out of the band of latitude $\pm 5^{\circ}$ around the equator; fourth row, j to l). A ratio of 1/2 means that that the energies are equal. Note the decimal logarithmic color scale for all the panels.

435 the semidiurnal band. By construction, wave drag primarily affects propagating tides and this energy reduction is to be expected. Yu et al. (2019) reported that the MITgcm tends to overestimate semidiurnal KE compared to surface drifters and, following

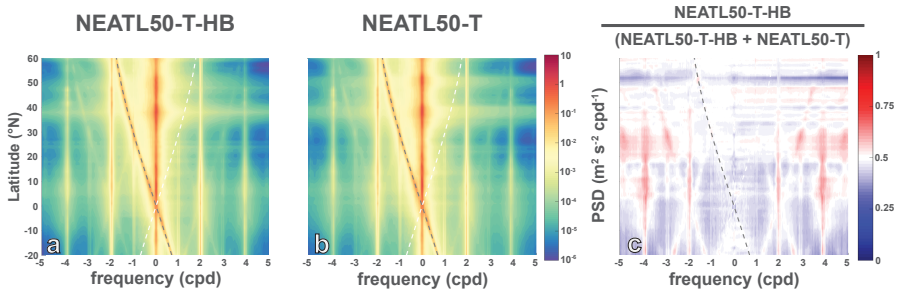


Figure 17. Zonally averaged rotary spectra in 1° latitude bins over regions in waters deeper than 500 m, in the NEATL domain for NEATL50-T-HB (a, first column), NEATL50-T (b, second column) and a normalized ratio obtained by dividing the first column by the sum of the first and second columns (c, last column). A ratio of 1/2 means that that the energies are equal. Note the decimal logarithmic color scale for the first and second columns.

Arbic et al. (2010) and Ansong et al. (2015), attributed this bias partly to the absence of topographic internal wave drag in the MITgcm simulations. Our results support this interpretation, with lower semidiurnal energy when wave drag is included. Moreover, the observed latitudinal pattern confirms that the inclusion of wave drag enhances barotropic tidal dissipation, consistent with the findings of Buijsman et al. (2015).

5.5 Bathymetry resolution

Chassignet et al. (2003) showed that the inclusion of high-resolution bathymetry can lead to a significant impact on the Gulf Stream pathway and variability. The NEATL50-T-HB and NEATL50-T experiments differ only by the higher resolution of the bathymetry in NEATL50-T-HB (see Chassignet et al. (2023) for details). Overall, increasing the bathymetry resolution leads to a reduction in energy in most of the frequency domain (Figure 17). However, notable exceptions are in the semidiurnal and higher-frequency tidal peaks, and the latitudinal band between 20°N and 30°N, where the KE is higher in the high-resolution bathymetry simulation. Table 2 confirms that the total energy decreases when the bathymetry resolution is increased from 1/12° to 1/50°. In the open ocean, the distribution between high and low frequencies remains consistent (Table 3). However, in shallow regions, a slight reduction in energy transfer to low frequencies is observed—accounting for 45% rather than the previous 49.7%. There are minimal changes in the diurnal and near-inertial components but enhancing the bathymetry resolution leads to an increased energy in the semidiurnal frequency band. The percentage of KE contained in the semidiurnal band increased from 2% to 2.5% in the shelf domain, and from 43.4% to 48.1% in the offshore domain when high-resolution bathymetry was used.

To assess the regional differences, KE maps are presented in Figure 18. Examining the KE maps (Figure 18), we find that the increase in bathymetry resolution does not have a clear impact on the energy for low-frequency and near-inertial bands, as both patches of higher and lower frequency are present. This could indicate, as examined for the Gulf Stream by Chassignet and Xu (2021) and Chassignet et al. (2023), a change in circulation patterns rather than a direct impact on the energy itself. With

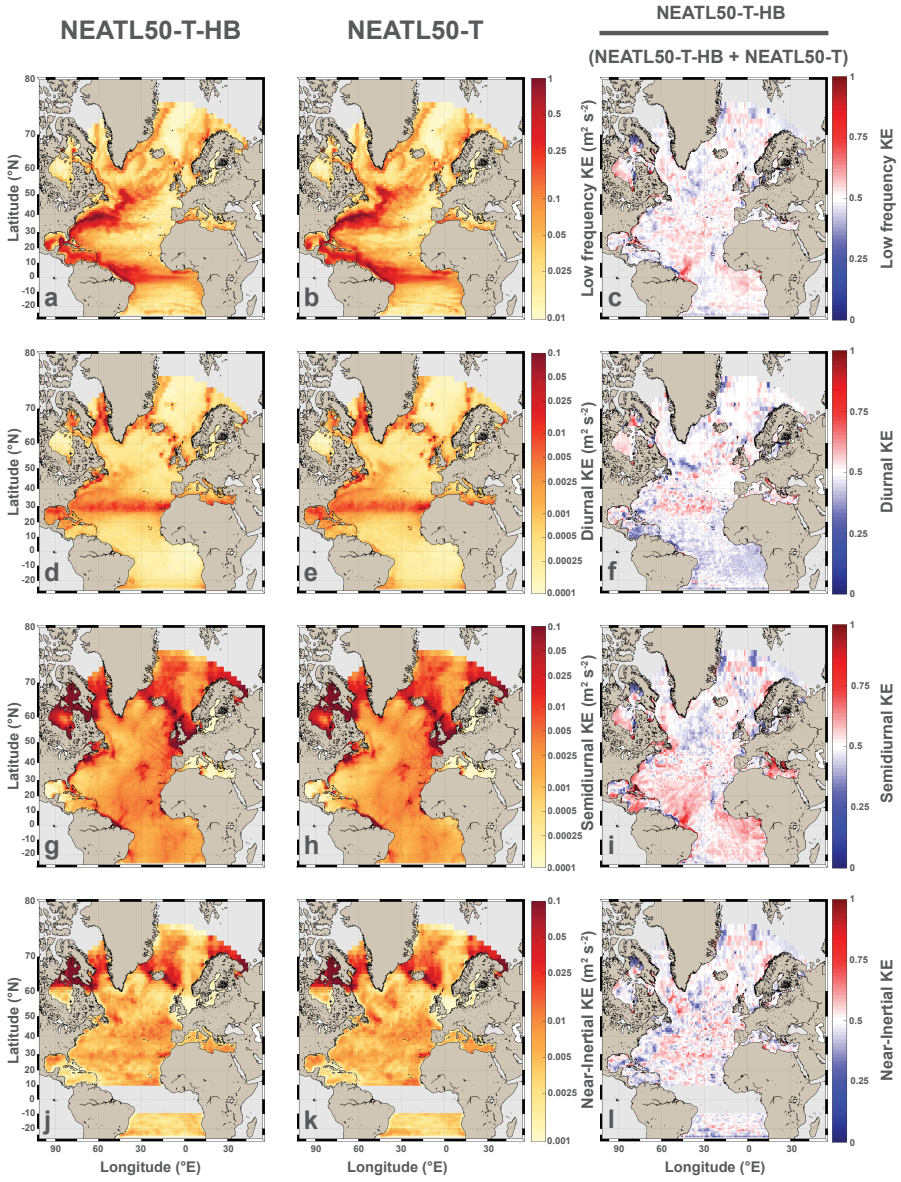


Figure 18. Maps of kinetic energy (KE) components in the NEATL domain for NEATL50-T-HB (first column), NEATL50-T (second column) and a normalized ratio obtained by dividing the first column by the sum of the first and second columns (last column). Maps of low-frequency ($>$ -0.5 cpd and $<$ 0.5 cpd; second row, a to c); Maps of diurnal ($\pm$[0.9, 1.1] cpd; third row, d to f); Maps of semidiurnal ($\pm$[1.9, 2.1] cpd; third row, g to i) and Maps of near-inertial ($\pm$[0.9, 1.1]f cpd out of the band of latitude $\pm 5^{\circ}$ around the equator; third row, j to l). A ratio of 1/2 means that that the energies are equal. Note the decimal logarithmic color scale for all the panels.

the exception of 30°N and a few specific regions such as the Adriatic Sea, the higher-resolution bathymetry tends to reduce energy in the diurnal frequency band. In contrast, in the semidiurnal band, the increase in bathymetry resolution increases the

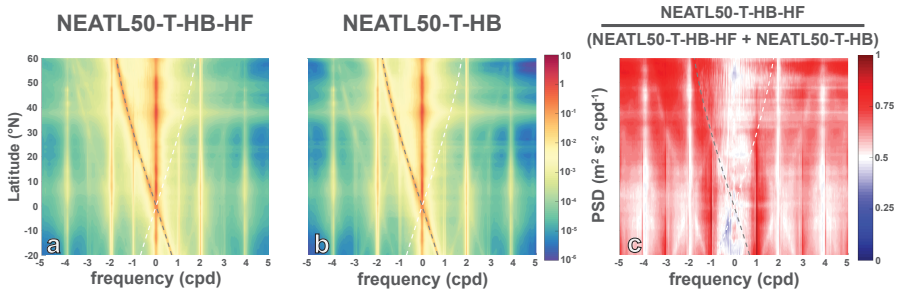


Figure 19. Zonally averaged rotary spectra in 1° latitude bins over regions in waters deeper than 500 m, in the NEATL domain for NEATL50-T-HB-HF (a, first column), NEATL50-T-HB (b, second column) and a normalized ratio obtained by dividing the first column by the sum of the first and second columns (c, last column). A ratio of 1/2 means that that the energies are equal. Note the decimal logarithmic color scale for the first and second columns.

surface KE, with a few exceptions, mainly at high latitudes. There is a clear increase in the KE associated with semidiurnal internal tides in the Amazon Shelf. A higher-resolution bathymetry product resolves more topographic gradients, leading to higher barotropic-to-baroclinic tidal conversion, and subsequent increase in semidiurnal tides KE, in agreement with Xu et al. (2022).

In conclusion, increasing the bathymetry resolution slightly decreases the energy and, as discussed by Chassignet and Xu (2021) and Chassignet et al. (2023), can lead to changes in large-scale circulation patterns, as indicated by both local increases or decreases of KE for low-frequency motions. The increase in bathymetry resolution also tends to reduce the energy of the diurnal peak, but increase that for the semidiurnal peak and tidal peaks at higher frequencies.

5.6 Temporal frequency of atmospheric forcing

Table 2 compares NEATL50-T-HB-HF and NEATL50-T-HB experiments, which differ only in the temporal frequency of the wind forcing (higher in NEATL50-T-HB-HF). Increasing the wind-forcing frequency leads to an overall rise in surface KE across all frequency bands. The increase is seen in both the open ocean and on the continental shelf. However, this increase is not uniform. For example, there is a reduced fraction of total to low frequencies in the offshore domain (86.7% instead of 91.4%) while it remains comparable close to the coasts (44.8% instead of 45.0%) (Table 3). At high frequencies, the energy in the diurnal and offshore near-inertial bands shows a large increase by more than 50%. This is also visible in Figure 19 where zonally averaged rotary spectra are compared. We find that an increase in wind frequency increases the energy in nearly all the frequency domains at all latitudes, with the exception of low and semidiurnal frequency motions where the level of energy is comparable. While there is also an increase on the shelf in the near-inertial band (Table 2), it is considerably less pronounced and comparable to the total increase of energy (Table 3).

To assess the regional differences, KE maps are presented in Figure 20. Examining these maps, we find that the domain-averaged increase in energy for higher wind frequency is not evenly distributed, as in some regions, higher temporal frequency

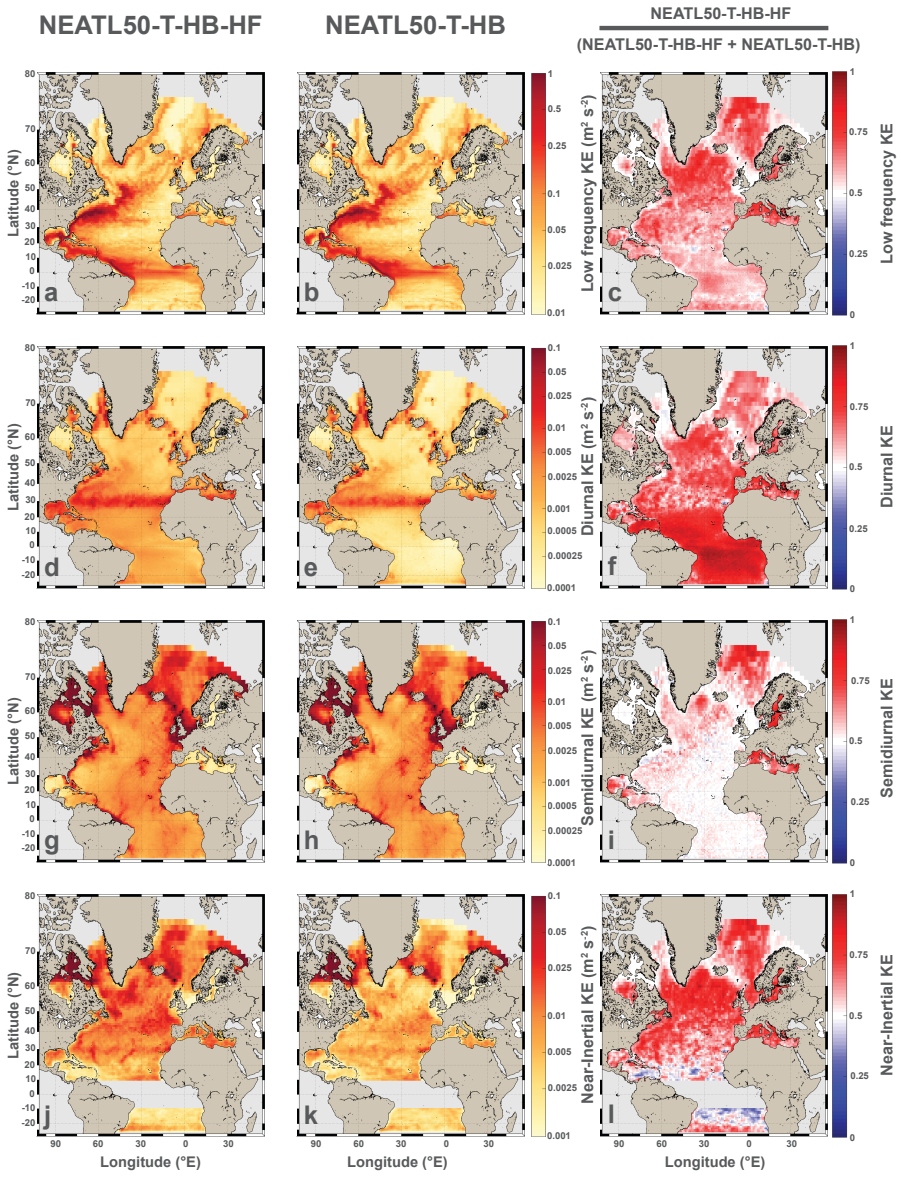


Figure 20. Maps of kinetic energy (KE) components in the NEATL domain for NEATL50-T-HB-HF (first column), NEATL50-T-HB (second column) and a normalized ratio obtained by dividing the first column by the sum of the first and second columns (last column). Maps of low-frequency ($>$ -0.5 cpd and $<$ 0.5 cpd; first row, a to c); Maps of diurnal ($\pm$[0.9, 1.1] cpd; second row, d to f); Maps of semidiurnal ($\pm$[1.9, 2.1] cpd; third row, g to i) and Maps of near-inertial ($\pm$[0.9, 1.1]f cpd out of the band of latitude $\pm 5^{\circ}$ around the equator; fourth row, j to l). A ratio of 1/2 means that that the energies are equal. Note the decimal logarithmic color scale for all the panels.

of wind results in less energy. There is a clear increase of energy for both diurnal and near-inertial frequency bands. However, in the middle of the Atlantic, there is no large signal on the KE in the semidiurnal frequency band, but higher wind frequency leads

to significantly higher semidiurnal KE in closed seas such as the Gulf of Mexico, Mediterranean Sea, Baltic Sea, Norwegian Sea and Greenland Sea.

In conclusion, increasing the frequency of wind forcing increases the total KE and at high frequency across most of the domain. The large increase of KE for diurnal (3 times in off-shore) and near-inertial (nearly 2 times in off-shore) is expected as winds have a diurnal cycle and winds are one of the main sources of near-inertial motions (Klein et al., 2004; Rimac et al., 2013). However, as noted by Rimac et al. (2013) and Yu et al. (2019), the impact of increasing the wind frequency on near-inertial motions is less pronounced in tropical and subtropical regions than in mid-latitudes (lower right panel of Figure 20). There is also a marked increase of semidiurnal energy in closed sea.

6 Summary

In this paper, we investigated surface kinetic energy (KE) distributions in the North and Equatorial Atlantic (NEATL) using seven tide-resolving HYCOM experiments, one numerical Lagrangian simulation (Ocean Parcels, OP), and observations from surface drifters. For each comparison, we considered both absolute KE values and the fraction of total KE contained in different frequency bands. The latter isolates changes in spectral distribution from changes in overall energy; accordingly, all reported band percentages are fractions of total KE. The analysis proceeded in three steps.

First, a domain-wide comparison of rotary spectra from all datasets established the large-scale spectral structure and highlighted systematic differences between models and observations. All spectra showed the expected low-frequency dominance (Wunsch and Stammer, 1995; Ferrari and Wunsch, 2009; Morrow and Le Traon, 2012) and distinct tidal and near-inertial peaks, with horizontal resolution emerging as the main distinction between all simulations: the KE in the 1/50° numerical simulations were systematically closer to that of the observed drifters than the 1/12° simulations. The high-frequency continuum between tidal peaks, i.e., the so-called Garrett–Munk spectrum (Garrett, 1972; Garrett and Munk, 1975), was systematically higher in 1/50° simulations, consistent with the idea that nonlinear interactions of internal gravity waves progressively fill out this spectral band (e.g., Olbers, 1976; McComas and Bretherton, 1977). This behavior reflects the ability of higher-resolution simulations to resolve smaller-scale wave modes, which in turn increases the energy transferred into the continuum (Müller et al., 2015). Nevertheless, even the higher-resolution simulations underestimate the continuum energy relative to drifters. This mismatch cannot be explained solely by the Eulerian–Lagrangian distinction, and likely reflects both physical processes not fully represented in the models, such as parts of the wave–wave interaction cascade—and observational artifacts, because high-frequency variance in drifter records can be inflated by GPS/Argos positioning errors (Yu et al., 2019). In the open ocean, 80–95% of modeled KE lay at low frequencies versus 60–75% for drifters. There are not enough drifters to compare the observations to the models on the shelf, but there is a stronger high frequency imprint in the models inshore than offshore, with the low-frequency KE accounting for only 45–50% inshore versus 80–95% offshore.

Second, we focused on the Lagrangian versus Eulerian perspective. Comparisons between numerical and undrogued drifters showed that numerical particles (OP) contain less total energy, but with a higher fraction of the total energy in the semidiurnal band (from around 1.1-1.2% for undrogued surface drifters to 1.7% for OP) and in the near-inertial band (from around 5.5-5.7%

for undrogued surface drifters to 7.6-8.1% for OP). Subsampling OP trajectories to match the drifter density slightly decreased the estimated KE–by just a few percent–indicating that, in the NEATL, sampling heterogeneity of surface buoys has a minor impact on the KE; this supports the use of surface drifters as a suitable reference dataset for model–data comparisons. Finally, OP–Eulerian comparisons confirmed that Lagrangian spectra are smoother, with attenuated high-frequency peaks and energy redistributed into surrounding frequencies, consistent with previous observational and modeling studies (e.g., Caspar-Cohen et al., 2024; Zhang et al., 2024). In our simulations, this smoothing led to around 50% less semidiurnal energy in Lagrangian than Eulerian estimates offshore.

Third, we conducted a pairwise sensitivity analysis to quantify the effect of specific model parameters on KE in both offshore (waters deeper than $500\,m$) and shelf (waters shallower than $500\,m$) regions. For the total KE, the dominant offshore factor was horizontal resolution: moving from 1/12° to 1/50° increased offshore KE by about one third, while the increase was less pronounced in the shelf region. By contrast, increasing vertical levels from 32 to 96 raised the total KE in the shelf domain, but had a less pronounced impact in the offshore domain. Changes in bathymetry resolution and wind forcing each have a slight impact on total energy, albeit in opposite directions: an increase in bathymetry resolution leads to a decrease in total energy, while an increase in wind forcing results in an energy increase.

Overall, the increase in total energy is evenly distributed between the low-frequency reservoir and the remaining frequency domains. The only notable exception occurs when the wind forcing is increased from a 6-hour to a 1-hour interval. In this case, the percentage of total energy stored in low frequencies in the open ocean drops from 91.4% to 86.7%, marking the only experiment where this percentage falls below 90%. On the continental shelf, all the percentages consistently range between 45% and 50%.

For the diurnal frequency band, the most significant impact arises from the wind forcing. An increase in wind frequency doubles the fraction of total offshore energy contained in the diurnal band (from 1.1 to 2.4%) and, although less pronounced, also enhances it on the continental shelf (from 1.4 to 2.2%). This increase is expected near the diurnal critical latitude (around 30°N), where aliasing occurs between diurnal tides and near-inertial motions. However, the wind-frequency-induced enhancement of diurnal energy is not confined to the vicinity of the critical latitude but is observed across the entire NEATL domain. In contrast, considering only the M_2 instead of eight largest tidal constituents (K_1, O_1, P_1, Q_1, M_2, S_2, N_2, and K_2) reduces this fraction on the continental shelf (from 1.5 to 0.5%) but not so much in the offshore region (from 1.3 to 1.1%).

For the semidiurnal frequency band, the most notable effect is the increase in the fraction of total energy stored in both the inshore (43.4 to 48.5%) and offshore (2 to 2.5%) domains when the bathymetry resolution is increased. In contrast, and particularly in the offshore domain, the inclusion of a wave drag decreases the amount of energy stored (from 2% to 1.6%) in this band. Wave drag acts to reduce kinetic energy in all frequency bands equatorward of their respective critical latitudes and, because the semidiurnal critical latitude is located far poleward, this reduction is evident over nearly the entire domain. The decrease in semidiurnal energy associated with wave drag is consistent with the findings of Yu et al. (2019) and Arbic et al. (2022) who suggested that the absence of topographic internal wave drag can contribute to the overestimation of semidiurnal KE obtained with the MITgcm. Yu et al. (2019) also suggested that insufficient horizontal resolution could enhance energy in the semidiurnal band by promoting scattering into the wave continuum (Müller et al., 2015; Shriver et al., 2012). However, in

our experiments, increasing resolution did not lead to a higher fraction of offshore total energy in the semidiurnal band, and in the shelf domain; it actually resulted in a reduction in the fraction of total energy stored in this band.

Finally, for the near-inertial frequency band, primarily associated with anticyclonic motion, the most significant factor is the increase in wind forcing frequency, which nearly doubles the fraction of energy stored in this band in the open ocean (from 4.5 to 7.6%) and only slightly inshore (from 18.5 to 19.3%), consistent with winds being a major source of near-inertial motions (Klein et al., 2004; Rimac et al., 2013). As noted by Rimac et al. (2013) and Yu et al. (2019), this increase is less pronounced in tropical and subtropical regions than at mid-latitudes. In contrast, an increase in horizontal resolution, although associated with a higher absolute energy in this band due to the overall rise in total energy, reduces the fraction of total energy stored in the near-inertial band in the offshore region (from 6.1 to 4.2%) and in the shelf domain (20.3 to 18%).

Data availability. Surface velocity rotary spectra, averaged in $1° \times 1°$ bins over the HYCOM NEATL domain, together with total, low-frequency, diurnal, near-inertial, and semidiurnal kinetic energy diagnostics for the seven HYCOM simulations, the OceanParcels experiment, and the four drifter data sets (drogued or undrogued; all drifters or GPS only), are available at XXXXX (N.B. Will be a SEANOE Deposit (https://www.seanoe.org/) with a doi. During the review process, the netcdf can be found via https://fsu-my.sharepoint.com/:f:/g/personal/rlaxenaire_fsu_edu/IgD-oaEP7fnKSJsf4qNW5alaASoyqQ8emlOJjrbG3jsrEWU?e=NwGXbD).

Author contributions. RL, EC, BK, and FC conceived and proposed the idea for this study. XX ran the numerical simulations and the Ocean Parcel Experiments. RL did the analysis. RL and EC wrote the first draft of the manuscripts. All authors contributed to the writing and editing of the manuscript.

Competing interests. The authors declare that they have no conflict of interest.

Acknowledgements. Shane Elipot was supported by US National Science Foundation (NSF) Grants OCE-2242111 and OCE-1851166, Brian Arbic by the Office of Naval Research (ONR) Grant N00014-19-1-2712, Maarten Buijsman and Miguel Solano by the ONR Grant N00014-19-1-2704, and Eric Chassignet, Xiaobiao Xu, Alan Wallcraft, Luna Hiron, and Rémi Laxenaire by the ONR Grant N00014-19-1-2717.

References

Abdalla, S., Kolahchi, A. A., Ablain, M., Adusumilli, S., Bhowmick, S. A., Alou-Font, E., Amarouche, L., Andersen, O. B., Antich, H., Aouf, L., et al.: Altimetry for the future: Building on 25 years of progress, Advances in Space Research, 68, 319–363, https://doi.org/10.1016/j.asr.2021.01.022, 2021.

Ajayi, A., Le Sommer, J., Chassignet, E., Molines, J.-M., Xu, X., Albert, A., and Cosme, E.: Spatial and Temporal Variability of the North Atlantic Eddy Field From Two Kilometric-Resolution Ocean Models, Journal of Geophysical Research: Oceans, 125, e2019JC015 827, https://doi.org/10.1029/2019JC015827, 2020.

Ajayi, A., Le Sommer, J., Chassignet, E. P., Molines, J.-M., Xu, X., Albert, A., and Dewar, W.: Diagnosing Cross-Scale Kinetic Energy Exchanges From Two Submesoscale Permitting Ocean Models, Journal of Advances in Modeling Earth Systems, 13, e2019MS001 923, https://doi.org/10.1029/2019MS001923, 2021.

Amante, C. and Eakins, B.: ETOPO1 1 Arc-Minute Global Relief Model: procedures, data sources and analysis, NOAA Technical Memorandum NESDIS NGDC-24. National Geophysical Data Center, NOAA., https://doi.org/10.7289/V5C8276M, 2009.

Ansong, J. K., Arbic, B. K., Buijsman, M. C., Richman, J. G., Shriver, J. F., and Wallcraft, A. J.: Indirect evidence for substantial damping of low-mode internal tides in the open ocean, Journal of Geophysical Research: Oceans, 120, 6057–6071, https://doi.org/10.1002/2015JC010998, 2015.

Arbic, B. K.: Incorporating tides and internal gravity waves within global ocean general circulation models: A review, Progress in Oceanography, 206, 102 824, https://doi.org/10.1016/j.pocean.2022.102824, 2022.

Arbic, B. K., Wallcraft, A. J., and Metzger, E. J.: Concurrent simulation of the eddying general circulation and tides in a global ocean model, Ocean Modelling, 32, 175–187, https://doi.org/10.1016/j.ocemod.2010.01.007, 2010.

Arbic, B. K., Richman, J. G., Shriver, J. F., Timko, P. G., Metzger, E. J., and Wallcraft, A. J.: Global modeling of internal tides: Within an eddying ocean general circulation model, Oceanography, 25, 20–29, https://doi.org/0.5670/oceanog.2012.38, 2012.

Arbic, B. K., Alford, M. H., Ansong, J. K., Buijsman, M. C., Ciotti, R. B., Farrar, J. T., Hallberg, R. W., Henze, C. E., Hill, C. N., Luecke, C. A., et al.: A primer on global internal tide and internal gravity wave continuum modeling in HYCOM and MITgcm, New frontiers in operational oceanography, https://doi.org/10.17125/gov2018.ch13, 2018.

Arbic, B. K., Elipot, S., Brasch, J. M., Menemenlis, D., Ponte, A. L., Shriver, J. F., Yu, X., Zaron, E. D., Alford, M. H., Buijsman, M. C., et al.: Near-surface oceanic kinetic energy distributions from drifter observations and numerical models, Journal of Geophysical Research: Oceans, 127, e2022JC018 551, https://doi.org/10.1029/2022JC018551, 2022.

Archer, M., Wang, J., Klein, P., Dibarboure, G., and Fu, L.-L.: Wide-swath satellite altimetry unveils global submesoscale ocean dynamics, Nature, 640, 691–696, https://doi.org/10.1038/s41586-025-08722-8, 2025.

Baumann, T. M., Polyakov, I. V., Padman, L., Danielson, S., Fer, I., Janout, M., Williams, W., and Pnyushkov, A. V.: Arctic tidal current atlas, Scientific Data, 7, 275, https://doi.org/10.1038/s41597-020-00578-z, 2020.

Bleck, R.: An oceanic general circulation model framed in hybrid isopycnic-Cartesian coordinates, Ocean Modelling, 4, 55 – 88, https://doi.org/10.1016/S1463-5003(01)00012-9, 2002.

Buijsman, M. C., Arbic, B. K., Green, J., Helber, R. W., Richman, J. G., Shriver, J. F., Timko, P., and Wallcraft, A.: Optimizing internal wave drag in a forward barotropic model with semidiurnal tides, Ocean Modelling, 85, 42–55, https://doi.org/10.1016/j.ocemod.2014.11.003, 2015.

Buijsman, M. C., Stephenson, G. R., Ansong, J. K., Arbic, B. K., Green, J. M., Richman, J. G., Shriver, J. F., Vic, C., Wallcraft, A. J., and Zhao, Z.: On the interplay between horizontal resolution and wave drag and their effect on tidal baroclinic mode waves in realistic global ocean simulations, Ocean Modelling, 152, 101 656, https://doi.org/10.1016/j.ocemod.2020.101656, 2020.

Buijsman, M. C., Abdulfatai, M., Arbic, B. K., Chassignet, E. P., Hiron, L., Shriver, J. F., Solano, M., Varma, D., and Xu, X.: Energetics of (Super)Tidal Baroclinic Modes in a Realistically Forced Global Ocean Simulation, Journal of Geophysical Research: Oceans, 130, e2025JC022 460, https://doi.org/10.1029/2025JC022460, 2025.

Carnes, M. R.: Description and evaluation of GDEMV 3.0. Naval Rearch Laboratory Memo, Tech. rep., NRL/MR/7330-09-9165, 2009.

Caspar-Cohen, Z., Ponte, A., Lahaye, N., Carton, X., Yu, X., and Legentil, S.: Characterization of Internal Tide Incoherence: Eulerian versus Lagrangian Perspectives, Journal of Physical Oceanography, 52, 1245 – 1259, https://doi.org/10.1175/JPO-D-21-0088.1, 2022.

Caspar-Cohen, Z., Ponte, A., Lahaye, N., Zaron, E. d., Arbic, B. k., Yu, X., Legentil, S., and Menemenlis, D.: Combining surface drifters and high resolution global simulations enables the mapping of internal tide surface energ, Under Review at Scientific Reports., https://doi.org/10.21203/rs.3.rs-4583670/v1, 2024.

Chassignet, E. P. and Xu, X.: Impact of horizontal resolution (1/12 to 1/50) on Gulf Stream separation, penetration, and variability, Journal of Physical Oceanography, 47, 1999–2021, https://doi.org/10.1175/JPO-D-17-0031.1, 2017.

Chassignet, E. P. and Xu, X.: On the importance of high-resolution in large-scale ocean models, Advances in Atmospheric Sciences, 38, 1621–1634, https://doi.org/10.1007/s00376-021-0385-7, 2021.

Chassignet, E. P., Smith, L. T., Halliwell, G. R., and Bleck, R.: North Atlantic Simulations with the Hybrid Coordinate Ocean Model (HYCOM): Impact of the Vertical Coordinate Choice, Reference Pressure, and Thermobaricity, Journal of Physical Oceanography, 33, 2504–2526, https://doi.org/10.1175/1520-0485(2003)033<2504:naswth>2.0.co;2, 2003.

Chassignet, E. P., Hurlburt, H. E., Smedstad, O. M., Halliwell, G. R., Wallcraft, A. J., Metzger, E. J., Blanton, B. O., Lozano, C., Rao, D. B., Hogan, P. J., et al.: Generalized vertical coordinates for eddy-resolving global and coastal ocean forecasts, OCEANOGRAPHY-WASHINGTON DC-OCEANOGRAPHY SOCIETY-, 19, 118, https://doi.org/10.5670/oceanog.2006.95, 2006.

Chassignet, E. P., Hurlburt, H. E., Metzger, E. J., Smedstad, O. M., Cummings, J. A., Halliwell, G. R., Bleck, R., Baraille, R., Wallcraft, A. J., Lozano, C., Tolman, H. L., Srinivasan, A., Hankin, S., Cornillon, P., Weisberg, R., Barth, A., He, R., Werner, F., and Wilkin, J.: US GODAE: Global Ocean Prediction with the HYbrid Coordinate Ocean Model (HYCOM), Oceanography, 22, 64–75, https://doi.org/10.5670/oceanog.2009.39, 2009.

Chassignet, E. P., Yeager, S. G., Fox-Kemper, B., Bozec, A., Castruccio, F., Danabasoglu, G., Kim, W. M., Koldunov, N., Li, Y., and Lin, P.: Impact of horizontal resolution on global ocean-sea-ice model simulations based on the experimental protocols of the Ocean Model Intercomparison Project phase 2 (OMIP-2), Geoscientific Model Development Discussions, 2020, 1–58, https://doi.org/10.5194/gmd-13-45952020, 2020.

Chassignet, E. P., Xu, X., Bozec, A., and Uchida, T.: Impact of the New England seamount chain on Gulf Stream pathway and variability, Journal of Physical Oceanography, 53, 1871–1886, https://doi.org/10.1175/JPO-D-23-0008.1, 2023.

Chelton, D. B., Schlax, M. G., and Samelson, R. M.: Global observations of nonlinear mesoscale eddies, Progress in Oceanography, 91, 167–216, https://doi.org/10.1016/j.pocean.2011.01.002, 2011.

Davis, R.: Oceanic property transport, Lagrangian particle statistics, and their prediction, Journal of Marine Research, 41, 163–194, 1983.

Delandmeter, P. and Van Sebille, E.: The Parcels v2. 0 Lagrangian framework: new field interpolation schemes, Geoscientific Model Development, 12, 3571–3584, https://doi.org/10.5194/gmd-12-3571-2019, 2019.

Elipot, S. and Lumpkin, R.: Spectral description of oceanic near-surface variability, Geophysical Research Letters, 35, https://doi.org/10.1029/2007GL032874, 2008.

Elipot, S., Lumpkin, R., Perez, R. C., Lilly, J. M., Early, J. J., and Sykulski, A. M.: A global surface drifter data set at hourly resolution, Journal of Geophysical Research: Oceans, 121, 2937–2966, https://doi.org/10.1002/2016JC011716, 2016.

Elipot, S., Sykulski, A., Lumpkin, R., Centurioni, L., and Pazos, M.: Hourly location, current velocity, and temperature collected from Global Drifter Program drifters world-wide, Accession, 248584, v1, https://doi.org/10.25921/x46c-3620, 2022.

Emery, W. J. and Thomson, R. E.: Data Analysis Methods in Physical Oceanography (Second and Revised ed.), Elsevier, 2001.

Ferrari, R. and Wunsch, C.: Ocean circulation kinetic energy: Reservoirs, sources, and sinks, Annual Review of Fluid Mechanics, 41, https://doi.org/10.1146/annurev.fluid.40.111406.102139, 2009.

Fu, L.-L., Pavelsky, T., Cretaux, J.-F., Morrow, R., Farrar, J. T., Vaze, P., Sengenes, P., Vinogradova-Shiffer, N., Sylvestre-Baron, A., Picot, N., and Dibarboure, G.: The Surface Water and Ocean Topography Mission: A Breakthrough in Radar Remote Sensing of the Ocean and Land Surface Water, Geophysical Research Letters, 51, e2023GL107 652, https://doi.org/10.1029/2023GL107652, 2024.

Furevik, T. and Foldvik, A.: Stability at M2 critical latitude in the Barents Sea, Journal of Geophysical Research: Oceans, 101, 8823–8837, https://doi.org/10.1029/96JC00081, 1996.

Garrett, C.: Tidal resonance in the Bay of Fundy and Gulf of Maine, Nature, 238, 441–443, https://doi.org/10.1038/238441a0, 1972.

Garrett, C. and Munk, W.: Space-time scales of internal waves: A progress report, Journal of Geophysical Research, 80, 291–297, https://doi.org/10.1029/JC080i003p00291, 1975.

GEBCO: GEBCO Compilation Group, https://doi.org/10.5285/836f016a-33be-6ddc-e053-6c86abc0788e, 2019.

Goerss, J. S. and Jeffries, R. A.: Assimilation of synthetic tropical cyclone observations into the Navy Operational Global Atmospheric Prediction System, Weather and forecasting, 9, 557–576, https://doi.org/10.1175/1520-0434(1994)009<0557:AOSTCO>2.0.CO;2, 1994.

Gonella, J.: A rotary-component method for analysing meteorological and oceanographic vector time series, 19, 833–846, https://doi.org/10.1016/0011-7471(72)90002-2, 1972.

Gouillon, F., Morey, S. L., Dukhovskoy, D. S., and O'Brien, J. J.: Forced tidal response in the Gulf of Mexico, Journal of Geophysical Research: Oceans, 115, https://doi.org/10.1029/2010JC006122, 2010.

Grace, S. F.: The Principal Diurnal Constituent of Tidal Motion in the Gulf of Mexico., Geophysical Journal International, 3, 70–83, https://doi.org/10.1111/j.1365-246X.1932.tb00401.x, 1932.

Hiron, L., Schönau, M. C., Raja, K. J., Chassignet, E. P., Buijsman, M. C., Arbic, B. K., Bozec, A., Coelho, E. F., and Solano, M. S.: The Influence of Vertical Resolution on Internal Tide Energetics and Subsequent Effects on Underwater Acoustic Propagation, Journal of Advances in Modeling Earth Systems, 17, e2024MS004 389, https://doi.org/10.1029/2024MS004389, e2024MS004389 2024MS004389, 2025.

Hogan, T. F. and Rosmond, T. E.: The description of the Navy Operational Global Atmospheric Prediction System's spectral forecast model, Monthly Weather Review, 119, 1786–1815, https://doi.org/10.1175/1520-0493(1991)119<1786:TDOTNO>2.0.CO;2, 1991.

Jayne, S. R. and St. Laurent, L. C.: Parameterizing tidal dissipation over rough topography, Geophysical Research Letters, 28, 811–814, https://doi.org/10.1029/2000GL012044, 2001.

Jänicke, L., Ebener, A., Dangendorf, S., Arns, A., Schindelegger, M., Niehüser, S., Haigh, I. D., Woodworth, P., and Jensen, J.: Assessment of Tidal Range Changes in the North Sea From 1958 to 2014, Journal of Geophysical Research: Oceans, 126, e2020JC016 456, https://doi.org/10.1029/2020JC016456, 2021.

Klein, P., Lapeyre, G., and Large, W. G.: Wind ringing of the ocean in presence of mesoscale eddies, Geophysical Research Letters, 31, https://doi.org/10.1029/2004GL020274, 2004.

Lange, M. and Van Sebille, E.: Parcels v0. 9: prototyping a Lagrangian ocean analysis framework for the petascale age, Geoscientific Model Development, 10, 4175–4186, https://doi.org/10.5194/gmd-10-4175-2017, 2017.

Le Traon, P.-Y.: From satellite altimetry to Argo and operational oceanography: three revolutions in oceanography, Ocean Science, 9, 901–915, https://doi.org/10.5194/os-9-901-2013, 2013.

Lumpkin, R. and Pazos, M.: Measuring surface currents with Surface Velocity Program drifters: the instrument, its data, and some recent results, p. 39–67, Cambridge University Press, https://doi.org/10.1017/CBO9780511535901.003, 2007.

McComas, C. H. and Bretherton, F. P.: Resonant interaction of oceanic internal waves, Journal of Geophysical Research, 82, 1397–1412, https://doi.org/10.1029/JC082i009p01397, 1977.

Middleton, J. F.: Drifter spectra and diffusivities, Journal of marine research, 43, 37–55, 1985.

Middleton, J. H. and Denniss, T.: The propagation of tides near the critical latitude, Geophysical & Astrophysical Fluid Dynamics, 68, 1–13, https://doi.org/10.1080/03091929308203559, 1993.

Mooers, C. N.: A technique for the cross spectrum analysis of pairs of complex-valued time series, with emphasis on properties of polarized components and rotational invariants, 20, 1129–1141, https://doi.org/10.1016/0011-7471(73)90027-2, 1973.

Morrow, R. and Le Traon, P.-Y.: Recent advances in observing mesoscale ocean dynamics with satellite altimetry, Advances in Space Research, 50, 1062–1076, https://doi.org/10.1016/j.asr.2011.09.033, 2012.

Morrow, R., Fu, L.-L., Ardhuin, F., Benkiran, M., Chapron, B., Cosme, E., d'Ovidio, F., Farrar, J. T., Gille, S. T., Lapeyre, G., et al.: Global observations of fine-scale ocean surface topography with the Surface Water and Ocean Topography (SWOT) mission, Frontiers in Marine Science, 6, 232, https://doi.org/10.3389/fmars.2019.00232, 2019.

Müller, P., McWilliams, J., and Molemaker, M.: Routes to dissipation in the ocean: The 2D/3D turbulence conundrum, Marine turbulence: theories, observations and models, 397, 405, 2005.

Müller, M., Arbic, B. K., Richman, J. G., Shriver, J. F., Kunze, E. L., Scott, R. B., Wallcraft, A. J., and Zamudio, L.: Toward an internal gravity wave spectrum in global ocean models, Geophysical Research Letters, 42, 3474–3481, https://doi.org/10.1002/2015GL063365, 2015.

Nelson, A., Arbic, B., Menemenlis, D., Peltier, W., Alford, M., Grisouard, N., and Klymak, J.: Improved internal wave spectral continuum in a regional ocean model, Journal of Geophysical Research: Oceans, 125, e2019JC015 974, https://doi.org/10.1029/2019JC015974, 2020.

Niiler, P. P. and Paduan, J. D.: Wind-Driven Motions in the Northeast Pacific as Measured by Lagrangian Drifters, Journal of Physical Oceanography, 25, 2819 – 2830, https://doi.org/10.1175/1520-0485(1995)025<2819:WDMITN>2.0.CO;2, 1995.

Olbers, D. J.: Nonlinear energy transfer and the energy balance of the internal wave field in the deep ocean, Journal of Fluid mechanics, 74, 375–399, https://doi.org/10.1017/S0022112076001857, 1976.

Pugh, D. and Woodworth, P.: Tidal dynamics, p. 97–132, Cambridge University Press, 2014.

Raja, K. J., Buijsman, M. C., Shriver, J. F., Arbic, B. K., and Siyanbola, O.: Near-inertial wave energetics modulated by background flows in a global model simulation, Journal of Physical Oceanography, 52, 823–840, https://doi.org/10.1175/JPO-D-21-0130.1, 2022.

Rimac, A., von Storch, J.-S., Eden, C., and Haak, H.: The influence of high-resolution wind stress field on the power input to near-inertial motions in the ocean, Geophysical Research Letters, 40, 4882–4886, https://doi.org/10.1002/grl.50929, 2013.

Robertson, R.: Internal tides and baroclinicity in the Southern Weddell Sea: 2. Effects of the critical latitude and stratification, Journal of Geophysical Research: Oceans, 106, 27 017–27 034, https://doi.org/10.1029/2000JC000476, 2001.

Saha, S., Moorthi, S., Pan, H.-L., Wu, X., Wang, J., Nadiga, S., Tripp, P., Kistler, R., Woollen, J., Behringer, D., and et al.: The NCEP Climate Forecast System Reanalysis, Bulletin of the American Meteorological Society, 91, 1015–1058, https://doi.org/10.1175/2010bams3001.1, 2010.

Shriver, J. F., Arbic, B. K., Richman, J. G., Ray, R. D., Metzger, E. J., Wallcraft, A. J., and Timko, P. G.: An evaluation of the barotropic and internal tides in a high-resolution global ocean circulation model, Journal of Geophysical Research: Oceans, 117, https://doi.org/10.1029/2012JC008170, 2012.

Smith, W. and Sandwell, D.: Global Sea Floor Topography from Satellite Altimetry and Ship Depth Soundings, Science, 277, 1956–1962, https://doi.org/10.1126/science.277.5334.1956, 1997.

Teague, W. J., Carron, M. J., and Hogan, P. J.: A comparison between the Generalized Digital Environmental Model and Levitus climatologies, Journal of Geophysical Research: Oceans, 95, 7167–7183, https://doi.org/10.1029/JC095iC05p07167, 1990.

Uppala, S. M., Kållberg, P., Simmons, A. J., Andrae, U., Bechtold, V. D. C., Fiorino, M., Gibson, J., Haseler, J., Hernandez, A., Kelly, G., et al.: The ERA-40 re-analysis, Quarterly Journal of the Royal Meteorological Society: A journal of the atmospheric sciences, applied meteorology and physical oceanography, 131, 2961–3012, https://doi.org/10.1256/qj.04.176, 2005.

Villas Bôas, A. B., Marechal, G., and Bohé, A.: Observing Interactions Between Waves, Winds, and Currents From SWOT, Geophysical Research Letters, 52, e2024GL114 331, https://doi.org/10.1029/2024GL114331, 2025.

Webb, D. J.: On the shelf resonances of the English Channel and Irish Sea, Ocean Science, 9, 731–744, https://doi.org/10.5194/os-9-731-2013, 2013.

Wunsch, C. and Ferrari, R.: Vertical mixing, energy, and the general circulation of the oceans, Annu. Rev. Fluid Mech., 36, 281–314, https://doi.org/10.1146/annurev.fluid.36.050802.122121, 2004.

Wunsch, C. and Stammer, D.: The global frequency-wavenumber spectrum of oceanic variability estimated from TOPEX/POSEIDON altimetric measurements, Journal of Geophysical Research: Oceans, 100, 24 895–24 910, https://doi.org/10.1029/95JC017830, 1995.

Xu, X., Chassignet, E. P., Wallcraft, A. J., Arbic, B. K., Buijsman, M. C., and Solano, M.: On the spatial variability of the mesoscale sea surface height wavenumber spectra in the Atlantic Ocean, Journal of Geophysical Research: Oceans, 127, e2022JC018 769, https://doi.org/10.1029/2022JC018769, 2022.

Xu, X., Chassignet, E. P., and Wallcraft, A. J.: Impact of vertical resolution on representing baroclinic modes and water mass distribution in the North Atlantic, Ocean Modelling, 186, 102 261, https://doi.org/10.1016/j.ocemod.2023.102261, 2023.

Yu, X., Ponte, A. L., Elipot, S., Menemenlis, D., Zaron, E. D., and Abernathey, R.: Surface kinetic energy distributions in the global oceans from a high-resolution numerical model and surface drifter observations, Geophysical Research Letters, 46, 9757–9766, https://doi.org/10.1029/2019GL083074, 2019.

Zaron, E. D. and Elipot, S.: An assessment of global ocean barotropic tide models using geodetic mission altimetry and surface drifters, Journal of Physical Oceanography, 51, 63–82, https://doi.org/10.1175/JPO-D-20-0089.1, 2021.

Zhang, X., Yu, X., Ponte, A. L., Caspar-Cohen, Z., Le Gentil, S., Wang, L., and Gong, W.: Lagrangian Versus Eulerian Spectral Estimates of Surface Kinetic Energy Over the Global Ocean, Journal of Geophysical Research: Oceans, 129, e2024JC021 057, https://doi.org/doi.org/10.1029/2024JC021057, e2024JC021057 2024JC021057, 2024.